Soft Matter

Accepted Manuscript

This is an *Accepted Manuscript*, which has been through the Royal Society of Chemistry peer review process and has been accepted for publication.

Accepted Manuscripts are published online shortly after acceptance, before technical editing, formatting and proof reading. Using this free service, authors can make their results available to the community, in citable form, before we publish the edited article. We will replace this *Accepted Manuscript* with the edited and formatted *Advance Article* as soon as it is available.

You can find more information about *Accepted Manuscripts* in the Information for Authors.

Please note that technical editing may introduce minor changes to the text and/or graphics, which may alter content. The journal's standard Terms & Conditions and the Ethical guidelines still apply. In no event shall the Royal Society of Chemistry be held responsible for any errors or omissions in this *Accepted Manuscript* or any consequences arising from the use of any information it contains.

ROYAL SOCIETY OF CHEMISTRY

www.rsc.org/softmatter

We show that flowing multicomponent suspensions of deformable capsules display segregation based on shape. Theory shows excellent agreement with simulations.

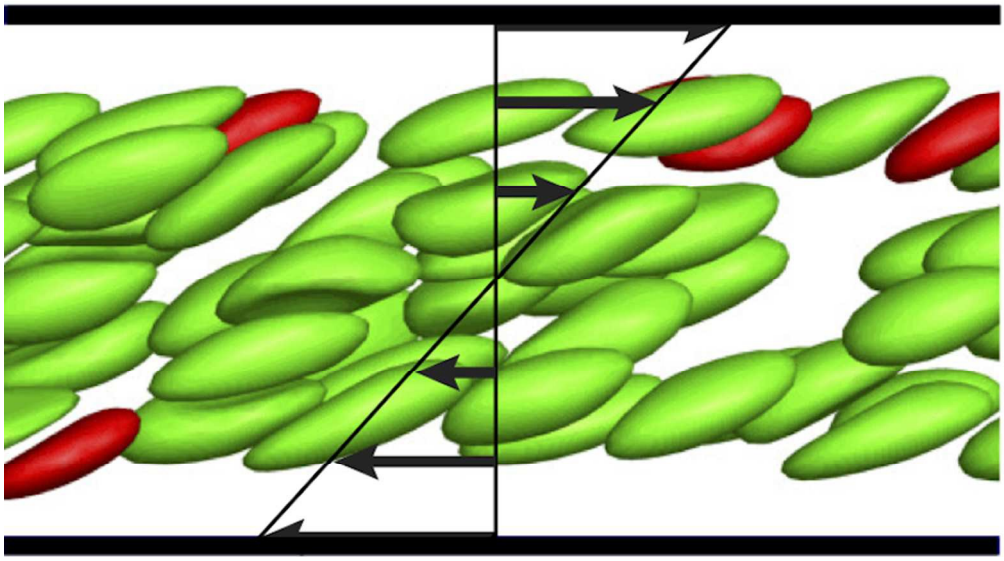

71x39mm (300 x 300 DPI)

Shape-mediated margination and demargination in flowing multicomponent suspensions of deformable capsules

Kushal Sinha and Michael D. Graham*

Department of Chemical and Biological Engineering

University of Wisconsin-Madison, Madison, WI 53706-1691

(Dated: December 1, 2015)

Abstract

We present detailed simulations and theory for flow-induced segregation in suspensions of deformable fluid-filled capsules with different shapes during simple shear flow in a planar slit. This system is an idealized model for transport for blood cells and/or drug carriers in the microcirculation or in microfluidic devices. For the simulations, an accelerated implementation of the boundary integral method was employed. We studied the binary mixtures of spherical and ellipsoidal capsules, varying the aspect ratio κ of the ellipsoid while keeping constant either (a) equatorial radius or (b) volume. Effects of a variety of parameters was studied, including κ, volume fraction and number fraction of the spherical capsules in the mixture. In suspensions where the ellipsoids have the same equatorial radius as the spheres, capsules with lower κ marginate. In suspension where the ellipsoids have the same volume as the spheres, ellipsoidal (both oblate and prolate) capsules are seen to demarginate in a mixture of primarily spherical capsules. To understand these results, a mechanistic framework based on the competition between wall-induced migration and shear-induced collisions is presented. A simplified drift-diffusion theory based on this framework shows excellent qualitative agreement with simulation results.

* Corresponding author. E-mail: mdgraham@wisc.edu

I. INTRODUCTION

Blood is a multicomponent suspension whose particulate components consist primarily of red blood cells (RBCs) along with trace amounts of other components such as leukocytes and platelets. The key physical differences between the leukocytes, platelets and RBCs are their relative shape, size and rigidity: RBCs are biconcave discoids, while the leukocytes are spherical and non-activated platelets are disk-like; the leukocytes are larger than RBCs, while the platelets are smaller; both are considerably stiffer than RBCs [1, 2]. Under physiological conditions, both the leukocytes and the platelets in blood segregate near the vessel wall [3, 4], a phenomenon known as margination, while the RBCs migrate away from the wall forming a so-called cell-free layer [1, 2]. Margination of leukocytes and platelets has substantial physiological significance in the processes of inflammation and hemostasis [3, 4]. Recent advances in lab-on-a-chip (LOC) technology and vascular-targeted carriers (VTCs) offer an unique opportunity to improve disease diagnosis and treatment by providing highly localized delivery of therapeutic agents. Understanding the segregation behavior of confined multicomponent suspensions as a function of physical parameters such as size, shape and deformability can provide explanations for experimental observations and guiding principles for design of LOC devices and VTCs. Recent work [5–7] has shed light on how particle size and membrane deformability affects segregation behavior and the mechanisms behind it; the role of particle shape is still poorly understood and is the focus of the present work.

The past decade has seen the emergence of particle shape as an important design parameter for controlling biological responses of drug delivery carriers [8–15]. The shape of drug delivery carriers have been shown to affect their blood circulation, phagocytosis, endocytosis and targeting [8, 16–18]. Studies of the margination and adhesion propensity with endothelial wall of ellipsoidal micro- and nanoparticles designed for vascular-targeted drug delivery has also shown shape as an important parameter [12, 13, 19]. The effect of particle shape on segregation has been characterized to some extent for suspension of rigid micro- and nanoparticles. Gentile *et al.* [12] observed that disk-shaped and hemi-spherical nanoparticles had higher "margination" propensity than spherical particles. However, what they observed is not margination *per se* but rather sedimentation of particles and particles of different shapes had different densities – their studies were of single-component suspensions without a dominant component playing the role that RBCs play in blood. Doshi *et*

al. [19] studied spherical particles of three different sizes; 1, 3 and 6 μm and elliptical disks, circular disks and rods stretched from them. They showed that adhesion propensity to endothelial wall in a synthetic microvascular network (SMN) increased with higher aspect ratio (prolateness increases with aspect ratio), with the difference amplifying at larger size and bifurcation junction. The walls of the SMN were coated with bovine serum albumin (BSA) while the particles were coated with anti-BSA antibody and increased adhesion of higher aspect ratio particles can be attributed to enhanced contact area provided by them for receptor-mediated adhesion than shape-induced localization near wall in single component system. In an *in vivo* study, Decuzzi *et al.* [20] showed that discoidal particles accumulate more than spherical, hemispherical or cylindrical particles in most organs aside from the liver, where cylindrical particles have the highest accumulation. Toy *et al.* [21] showed that gold nanorods marginate more than gold nanospheres. Mesoporous silicon particles of different shape were studied by Adriani *et al.* [22], who showed that disk-like particles showed the highest adhesion propensity.

The inspiration to use physical properties like shape to control biological function comes from biology itself where one can find, for example, a wide variety of bacterial shapes that enable specific functions [23]. Moreover, the biconcave discoid shape of RBCs is often attributed to the avoidance of filtration of RBCs in the spleen [24, 25]. In diseases such as sickle-cell anemia or malaria, RBCs tend to change their shape and several continuous shape-based separation techniques have been developed recently [26, 27] which could be used for their diagnosis. These separation techniques could be used for cell-sorting and purification as well. A recent discovery showing that proteins sense membrane curvature [28–31] has escalated the position of vesicle shape from a passive consequence of cellular activity to the prime player in cell growth, division and movement. These recent advancements and opportunities point to the need for a systematic understanding of shape-mediated flow-induced segregation in multicomponent suspensions.

It is important to note that all of the above-mentioned *in vitro* studies just described suffer from a major drawback; they did not consider margination in the presence of RBCs but rather examined only a single component in solution. This issue was recently experimentally addressed by Thompson *et al.* [13], who studied margination of spherical and ellipsoidal micro- and nanoparticles in reconstituted blood in a microfluidic chamber lined with human umbilical vein endothelial cells. They reported that ellipsoidal microparticles with high

aspect ratio showed higher margination compared to their spherical counterparts in both laminar and pulsatile flow. The results reported above are for rigid VTCs and suggest that rigid non-spherical particles with higher aspect ratio have a higher degree of margination compared to rigid spherical particles. Researchers [32, 33] have been able to develop non-spherical functional liquid-crystal deformable droplets which could be used as VTCs in future. We would like to remind readers that our own RBCs, WBCs and platelets are deformable as well. How shape would affect the segregation and margination of deformable particle is not characterized and is the focus of this work.

Recently, there have been some computational studies on the margination of particles in presence of the RBCs to complement the experimental studies noted above. Tan *et al.* [34] showed that RBCs enhance the margination of rigid spherical nanoparticles leading to higher binding. They also reported experimental observations validating results obtained in simulations. Müller *et al.* [35] found that margination of stiffer micro- and nanoparticles increases with increasing hematocrit and particle size. Spherical particles showed better margination than ellipsoidal particles; however ellipsoidal particles have slower rotational velocity in the cell-free layer which would result in higher binding seen in experiments. In a simulation of nanoparticles with binding affinity at wall in absence of RBCs, Tan *et al.* [36] showed that rods have higher binding than spherical particles which is dependent on their initial contact points and orientations to the wall. They also found higher concentration of nanoparticles in bifurcation region; an observation seen by Doshi *et al.* [19] in their experiments. Apart from studies of nanoparticles of various shapes in both presence and absence of RBCs, a number of computational studies have addressed leukocyte margination [37–39] and platelet margination [40–43] in presence of RBCs, where authors varied size, shape and membrane deformability altogether to study margination behavior. The absence of a systematic variation of shape of deformable particles, which is critical for understanding its role in the margination behavior and underlying mechanism, provides motivation for the present work.

Relative deformability, size and shape are the primary physical properties that determine segregation behavior in multicomponent suspensions. How each of these physical properties alone lead to segregation behavior is still very poorly understood. Past direct simulation studies that focus on the margination of platelets [40, 41], leukocytes [38, 39] and drug delivery particles [34, 44] suffer from a major drawback that the individual components differ

simultaneously in size, shape and membrane deformability. Moreover, in these studies, one component is always very dilute – the effect of the fraction of individual components in a mixture on the overall segregation behavior has not been thoroughly explored.

A series of controlled computational studies on the effect of deformability and size on margination was recently done [5, 7, 45]. The role of membrane deformability alone was investigated [5, 7] in plane Poiseuille flow and simple shear flow respectively, of a binary suspension of neo-Hookean capsules. In both flow situations, when stiffer particles are dilute in suspension, they undergo margination. However, when flexible particles are the dilute component, they enrich around the centerline, a phenomenon termed "demargination". The effect of particle size was also studied [7]. When small particles are dilute in suspension, they undergo margination. On the other hand, when large particles are the dilute component, they demarginate.

To explain the observations of size and membrane deformability, these authors proposed a qualitative mechanism [5] incorporating the two key sources of wall-normal particle motion in confined suspensions: (i) wall-induced hydrodynamic migration away from the wall; (ii) hydrodynamic pair collisions. In multicomponent suspensions, two types of pair collisions occur: (a) homogeneous collisions, which are between two particles of the same type and (b) heterogeneous collisions, which are between two particles of different type. Pair collision studies showed that stiff or small particles had larger post-collisional cross-stream displacement than flexible or large particles in a heterogeneous pair collision, while the displacements in homogeneous collisions of either species were between these two limits. They looked into the escape tendency of the dilute component in the near wall region and suggested that larger cross-stream displacement of stiff (or small) particle in heterogeneous collision compounded by their slower migration velocity than flexible (or big) particle will pose a stronger barrier for their escape to the bulk region leading to margination of the component. By the same argument, demargination was suggested to occur for flexible (or big) particles in suspensions of primarily stiff (or small) particles. They introduced an idealized master equation (ME) model – a set of integrodifferential equations – and employed a novel hydrodynamic Monte Carlo (HMC) simulation technique to solve it [6]. (See [46, 47] for related studies of single-component confined suspensions.) The ME model incorporates both sources of wall-normal particle motion and the HMC approach allows delineation of the role of each of these sources in the segregation behavior. In the case of segregation by deformability at constant size, it

was shown that at low volume fraction, heterogeneous collisions lead to segregation while at higher volume fractions both wall-induced migration and heterogeneous collisions have comparable contributions, while in size segregation the difference in migration velocities is dominant [7]. Approximating the collisions as small and occurring only between particles on nearby streamlines and considering a binary suspension where one component is present only in trace amounts, Henríquez *et al.* [48] reduced the ME model to a pair of differential equations in drift-diffusion form – we denote this as the "simplified drift-diffusion" (SDD) model. In simple shear, this model is analytically solvable, and the solution for the trace component contains a "margination parameter" M, which incorporates the migration and collision parameters and whose value determines the segregation behavior. If $M < 1$ then the trace component marginates; otherwise it demarginates. Additionally, if $M < -1$ then all particles of the trace component are driven to the wall, complete "drainage" of the trace component from the bulk suspension is predicted. In the present work we apply this model to shape segregation, showing that it qualitatively captures the observed simulation results.

In light of the above discussion, the aim of the present work is to investigate segregation behavior during plane Couette flow in binary suspensions of elastic capsules where the components differ in shape alone. This study complements prior studies of the elastic capsule model that focused on segregation by size and deformability [5–7, 45, 48]. While the elastic capsule model does not capture all aspects of cell properties and dynamics, this disadvantage is outweighed by the ability to use this model to separately consider effects of size, deformability and shape contrast on the margination process. As will be illustrated in Sections IV-V, margination can be understood based on a small number of general processes that are applicable regardless of the details of the system at hand.

The setup, formulation and numerical methods are detailed in Sec. II. Detailed results on the effect of relative concentration of individual components, aspect ratio and volume fraction on segregation of capsules of different shapes is presented in Sec. III. A mechanistic understanding based on the two key sources of wall-normal capsule motion is then provided in Sec. IV, providing insight into the segregation behavior seen in Sec. III. Finally, in Sec. V, we extend the SDD theory [48] to explain the shape-mediated segregation seen in our results.

II. PROBLEM FORMULATION AND IMPLEMENTATION

A. Overview

We consider here a suspension of deformable fluid-filled elastic capsules confined between two parallel plates as shown in Fig. 1 and subjected to simple shear flow with shear rate $\dot{\gamma}$. Simple shear flow was intentionally chosen to isolate the effect of shear on margination. Shear and how it mediates hydrodynamic interactions between cells and walls is the dominant effect near blood vessel walls even in the case of pressure-driven flows. Only near the channel center, where wall effects cancel out, does the gradient in shear rate present in pressure-driven flow play a substantial role in dynamics of deformable-particle suspensions, as has been demonstrated for stiffness segregation in prior computational work [5]. For this slit geometry, periodic boundary conditions are applied in x and z directions with spatial periods L_x and L_z, respectively (Fig. 1). In the y direction, no-slip velocity boundary conditions are applied at the two walls $y = 0$ and $y = 2H$ (Fig. 1). Both the suspending fluid and the fluid enclosed by the capsules are Newtonian and incompressible with the same viscosity μ and density ρ, i.e. the viscosity ratio $\lambda = 1$ is unity and the capsules are neutrally buoyant.

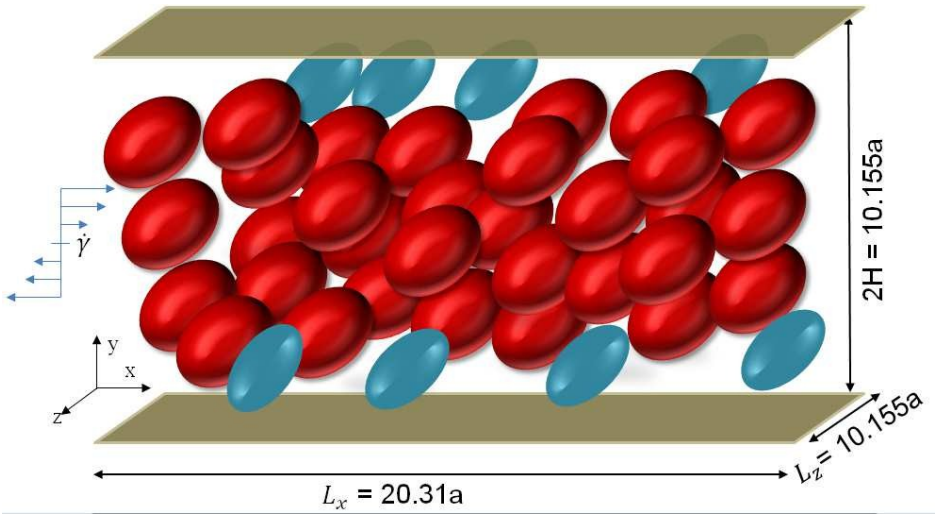

FIG. 1: Schematic of a binary suspension of spherical (in red) and ellipsoidal (in blue) capsules subjected to simple shear flow in a planar slit with height 2H.

A binary suspension of capsules with spherical and axisymmetric ellipsoidal (spheroidal) rest shapes is considered. The two broad cases considered in this work are: (i) ellipsoidal capsules having the same equatorial radius a as the radius a_s of spherical capsules, and (ii) ellipsoidal capsules having the same volume V as the volume V_s of the spherical capsules.

Shape is changed by varying aspect ratio $\kappa = b/a$, where b and a are the polar and equatorial radii (or semi-axes), respectively. Thus, $\kappa < 1$ and $\kappa > 1$ represent oblate and prolate, respectively. In case (i), the volume of the ellipsoidal capsules $V = \kappa V_s$, while in case (ii), the equatorial radius of the ellipsoidal capsules is $a = (a_s/\kappa)^{1/3}$. The non-dimensional capillary number $\mathrm{Ca} = \mu\dot{\gamma}a/G_c$ measures the ratio of viscous and elastic stresses on the capsule, where a is the equatorial radius of the capsule of interest and G_c is the surface shear modulus of the capsule membrane. The capillary number is kept constant at $\mathrm{Ca} = 0.5$ for both components in all simulations. At $\mathrm{Ca} = 0.5$ and $\lambda = 1$, spherical capsules are in tank-treading regime while ellipsoidal particles are in the swinging regime as indicated by single capsule simulations. Length is non-dimensionalized with a_s and time is non-dimensionalized with $\dot{\gamma}$. The scale of the cells and domain are taken to be small, so the Reynolds number $\mathrm{Re} = \rho\dot{\gamma}H^2/\mu$ is much less than unity.

We will use the letter 'S' to denote spherical particles, the letter 'P' to denote prolate particles, and the letter 'O' to denote oblate particles. The number fraction of the spherical capsules in a given suspension is denoted X_s. The number fraction of the oblate (or prolate) capsules can be obtained from X_s as: $X_o(\text{or } X_p) = 1 - X_s$. The suspension as a whole is characterized by its overall volume fraction ϕ. In the case of suspensions of spheres and constant-radius ellipsoids, as X_s changes the volume fraction will change (because the two components do not have the same volume). In this case, we will report mixture volume fraction as ϕ_s which is the volume fraction when all capsules are spherical.

B. Capsule model and surface discretization

The capsule membranes follow the neo-Hookean model. The strain-energy density W of the membrane in this case can be expressed as function of the principal stretch ratios, λ_1 and λ_2 [49]:

$$W = \frac{G_c}{2}\left[I_1 - 1 + \frac{1}{I_2 + 1}\right] \tag{1}$$

where I_1 and I_2 are given by

$$I_1 = \lambda_1^2 + \lambda_2^2 - 2, \quad I_2 = \lambda_1^2\lambda_2^2 - 1. \tag{2}$$

The elastic forces in the membrane are computed using the finite element approach of Charrier *et al.* [50], which is based on the principle of virtual work. Implementation details of this approach can be found in [51, 52]. The surface of each capsule is discretized into N_Δ triangular elements with linear basis functions employed over each element. In the present study, we took $N_\Delta = 320$, corresponding to 162 discretization nodes. As shown earlier [5], very long simulation times are required to reach steady state, and this mesh resolution keeps the computational time requirement manageable.

The computation of the boundary integral in Eq. 3 discussed below, requires the knowledge of the hydrodynamic traction jump across the interface ($\Delta\mathbf{f}$). This is obtained from the membrane equilibrium condition, which requires that the hydrodynamic forces on any infinitesimal area of the membrane balance by the elastic forces in the membrane. Hence $\Delta\mathbf{f}$ can be obtained from the knowledge of the elastic stresses. In the model used here, there is no bending resistance of the capsule membrane. In this case compressive stresses in the membrane can lead to membrane buckling. To circumvent this problem, capsules were slightly pre-inflated following the work of [53] with inflation ratio $I = a/a_0 - 1$, where the rest radius a of the capsule of interest is larger than the unstressed radius a_0. Here we set $I = 0.1$ as in previous studies [5, 45] and did not observe any buckling instabilities. Note that preinflation can also arise naturally in experiments due to osmotic effects [54]. Prior work has shown that aside from preventing buckling instabilities of the membrane, the effect of preinflation on dynamics is small [53].

C. Fluid velocity calculation: Boundary integral method

The Reynolds number for the problem is sufficiently small so that the fluid motion is assumed to be governed by the Stokes equation. Under these assumptions, one may write the fluid velocity $\mathbf{u}$ at any point $\mathbf{x}_0$ in the domain as [55]:

$$u_j(\mathbf{x}_0) = u_j^\infty(\mathbf{x}_0) - \frac{1}{8\pi\mu}\sum_{n=1}^{N_p}\int_{S^n}\Delta f_i(\mathbf{x})\,G_{ji}(\mathbf{x}_0,\mathbf{x})\,dS(\mathbf{x}) \tag{3}$$

where $\mathbf{u}^\infty(\mathbf{x}_0)$ is the undisturbed simple shear velocity at the point $\mathbf{x}_0$, S^n denotes the surface of capsule n, $\Delta\mathbf{f}(\mathbf{x})$ is the hydrodynamic traction jump across the interface, while $\mathbf{G}$ is the Green's function. Note that the sum in the above expression is over all the N_p capsules

in the system. A crucial aspect of the above formulation is that the Green's function $\mathbf{G}$ is taken to satisfy the boundary conditions imposed at the system boundaries, so the integrals above only involve the internal (interfacial) boundaries; if the Green's function for any other geometry is employed (e.g. free-space), additional integrals over the domain boundaries will arise in Eq. 3. The undisturbed flow velocity $\mathbf{u}^{\infty}$ is considered to be simple shear,

$$\mathbf{u}^{\infty}(x, y, z) = \dot{\gamma}(y - H)\mathbf{e}_x, \tag{4}$$

where H is the half-height of the channel (Fig. 1), and $\mathbf{e}_x$ is the unit vector in the x direction.

To determine the velocity field we use the accelerated boundary integral method of Kumar *et al.* [51] which is based on general geometry Ewald like method (GGEM) developed by Hernandez-Ortiz *et al.* [56]. The key idea in this approach is to split a Dirac-delta force density into a smooth quasi-Gaussian *global* density $\rho_g(\mathbf{r})$ and a second *local* density $\rho_l(\mathbf{r})$ given by the following expressions:

$$\rho_g(\mathbf{r}) = \frac{\alpha^3}{\pi^{3/2}} e^{-\alpha^2 r^2} \left(\frac{5}{2} - \alpha^2 r^2 \right), \tag{5a}$$

$$\rho_l(\mathbf{r}) = \delta(\mathbf{r}) - \rho_g(\mathbf{r}), \tag{5b}$$

where α^{-1} is the length scale over which the delta-function density $\delta(\mathbf{r})$ has been smeared using the quasi-Gaussian form above, while $\mathbf{r}$ is the position vector relative to the pole of the singularity. The solution associated with the local density is known analytically, is short ranged and is neglected beyond a length scale of $\mathrm{O}(\alpha^{-1})$ from its pole. The analytical solution is obtained assuming a free-space boundary conditions while the solution associated with global density is computed numerically ensuring that the boundary condition associated with overall problem is satisfied [51, 56]. The periodic x and z directions are represented using Fourier series while a Chebyshev Galerkin scheme is used in the y direction. The number of corresponding modes in x, y and z directions are N_x, N_y and N_z, respectively. Based on extensive tests in [51], we set $\alpha h_m = 0.5$ to minimize numerical error. Here, h_m is mean mesh spacing associated with the global solution and α is taken as $4/a_s$. Kumar *et al.* [51] have shown that the computational cost associated with this method is $O(N \ln N)$ for the slit geometry, where N is proportional to the product of total number of capsules in system, N_p and the number of triangular elements N_Δ on the capsule surface.

TABLE I: Parameter specification in various simulations. For all simulations, the capillary number based on equatorial radius Ca is 0.5, the confinement ratio C is 5.08 and neo-Hookean membrane law is used.

Set	$Shape_1$	$Shape_2$	κ	X_s	a/a_s	V/V_s	ϕ_s
A	S	O	{0.4,0.6,0.75}	0 – 1	1	{0.4,0.6,0.75}	{0.05,0.1,0.15}
B	S	P	{1.33,1.5,1.63}	0 – 1	1	{1.33,1.5,1.63}	{0.05,0.1,0.15}
C	S	O	{0.25,0.3,0.4}	0 – 1	{1.59,1.49,1.36}	1	{0.05,0.1,0.15}
D	S	P	{1.63,1.8,2.0}	0 – 1	{0.85,0.82,0.79}	1	{0.05,0.1,0.15}

Each time step in the solution procedure begins with the computation of the hydrodynamic traction jump $\Delta\mathbf{f}$ – this is computed using the approach outlined above in Sec. II B. Following this, we compute the velocity at all surface element nodes using the scheme just described. The surface element nodes are then advanced in time using the second order explicit Adams-Bashforth method. The time step Δt is set adaptively to satisfy $\Delta t = 0.1\text{Ca}\, h$, where h is the minimum node to node distance (the closest nodes do not have to be on the same capsule) [51]. We employ an overlap correction procedure in an auxiliary step [51], which maintains a minimum separation $\delta_{min} = 0.025a_s$ between the surfaces of any two capsules. Briefly, a pair of overlapping capsules are moved apart along their line of center in z direction until δ_{min} is achieved. Several hundred to more than a thousand time (strain) units are required for the capsule distribution to reach a statistically stationary state.

Table I shows the set of simulations performed in this study with their specific choices of parameters. The domain is $20.31a_s \times 10.15a_s \times 10.15a_s$ in the x, y, and z directions for all these simulations. Thus, the confinement ratio $C = H/a_s$ for all sets of runs is 5.08. The total number of capsules is 24, 48 and 72 at $\phi = 0.05, 0.10$ and 0.15 respectively. As can be seen, we have performed four main sets of simulations denoted by A, B, C and D in the table. These sets of simulations address the effect of the number fraction of the spherical capsule X_s on the segregation behavior in combination with several other parameters including shape, equatorial radius and volume of the ellipsoidal capsules as well as volume fraction. Additionally, to examine the effect of box size, simulations for set A were repeated in a bigger box of size $20.31a_s \times 20.31a_s \times 10.15a_s$ with 96 capsules and $\phi_s = 0.10$. The box size effect was found to be negligible as seen in Fig. 14, which is presented in Sec. III C.

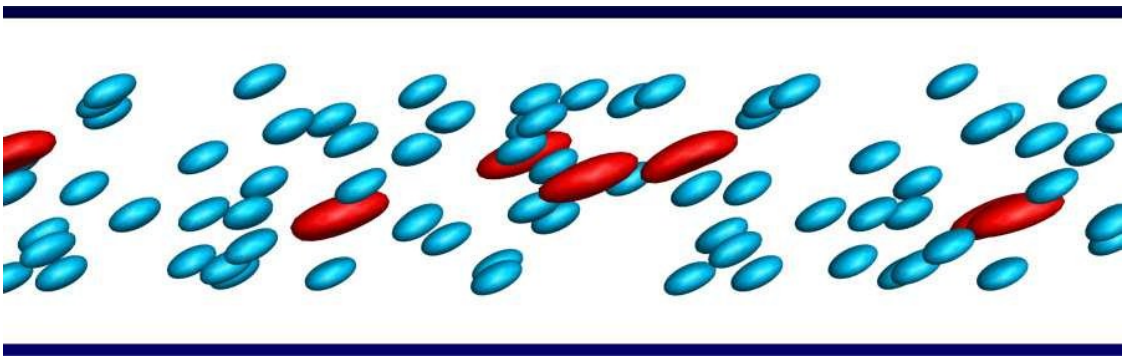

(a) $X_s = 0.1$

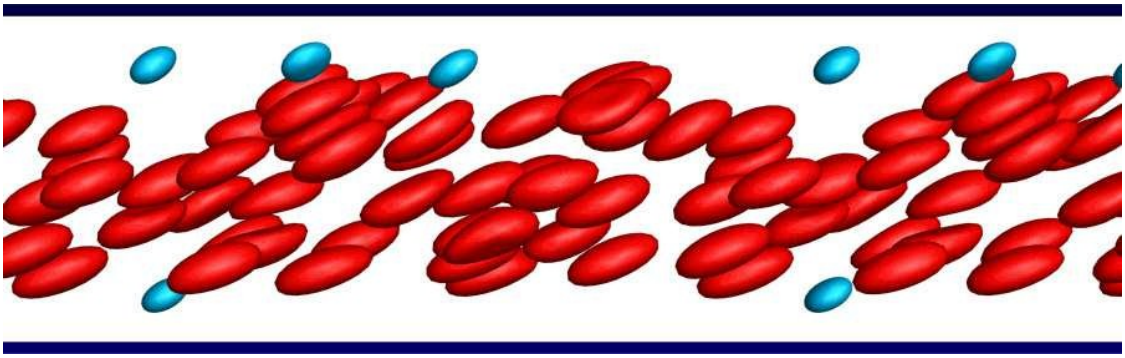

(b) $X_s = 0.9$

FIG. 2: Simulation snapshot for the mixture of oblate ($\kappa = 0.6$, blue) and spherical capsules (red) with (a) $X_s = 0.1$ and (b) $X_s = 0.9$. Both species have same equatorial radius with $\phi_s = 0.10$. Here and henceforth, we will represent oblate and spherical capsules by the colors blue and red, respectively.

III. RESULTS

A. Equatorial radius held constant

We begin this section with results for the case where both spherical and ellipsoidal capsules have the same equatorial radius. This case corresponds to simulation sets A and B in Table I. The volume of the ellipsoidal capsules varies linearly with aspect ratio κ and thus, the overall volume fraction ϕ will vary with X_s. The volume fraction at any X_s is $\phi = (X_s + \kappa(1 - X_s))\phi_s$ in these cases. We will first discuss the case $\phi_s = 0.10$ and the cases $\kappa = 0.6$ and $\kappa = 1.33$. Results for varying κ and ϕ_s are discussed later in Sec. III A 2. Simulation snapshots for different values of X_s are shown in Fig. 2 for set A and Fig. 3 for set B.

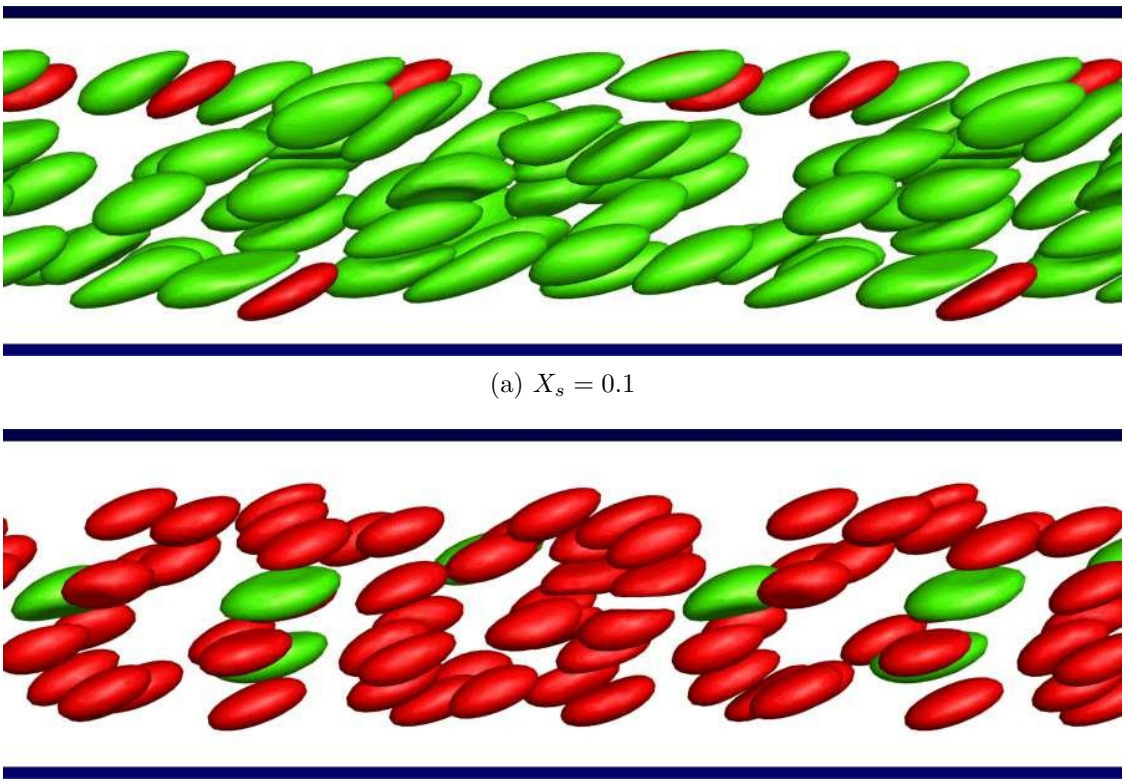

(a) $X_s = 0.1$

(b) $X_s = 0.9$

FIG. 3: Simulation snapshots for mixtures of prolate ($\kappa = 1.33$, green) and spherical capsules (red) with (a) $X_s = 0.1$ and (b) $X_s = 0.9$. Both species have same equatorial radius with $\phi_s = 0.10$. Here and henceforth, we will represent prolate capsules by the color green.

1. *Particle distribution in the wall normal direction*

The simplest way to examine segregation is to look into the steady state mean absolute distance of a species 'α' from the channel wall defined as $\bar{d}_\alpha = \langle\langle|y - y_{wall}|\rangle_{N_\alpha}\rangle_{t_s}$, where $\langle m\rangle_n$ represents the average of quantity m in the range of quantity n. Here, N_α is the number of capsules of species α and t_s is the time interval, after steady state is reached, in which temporal averaging is done, which is taken to be $t_s = 2000-3000$ for all the results presented in this work. It is noteworthy that steady state is typically reached after initial 1000 strains of the simulation.

We first consider the mixture of oblate and spherical capsules. From Fig. 4(a), we observe that $\bar{d}$ for both species decreases with the increase in X_s . This is expected as the $\bar{d}$ for the pure spherical capsule suspension is smaller than that for pure oblate capsules and the mixture will behave more like the spherical capsule case as X_s increases. We also observe that the oblate capsules stay closer to the wall and the margination tendency, quantified as

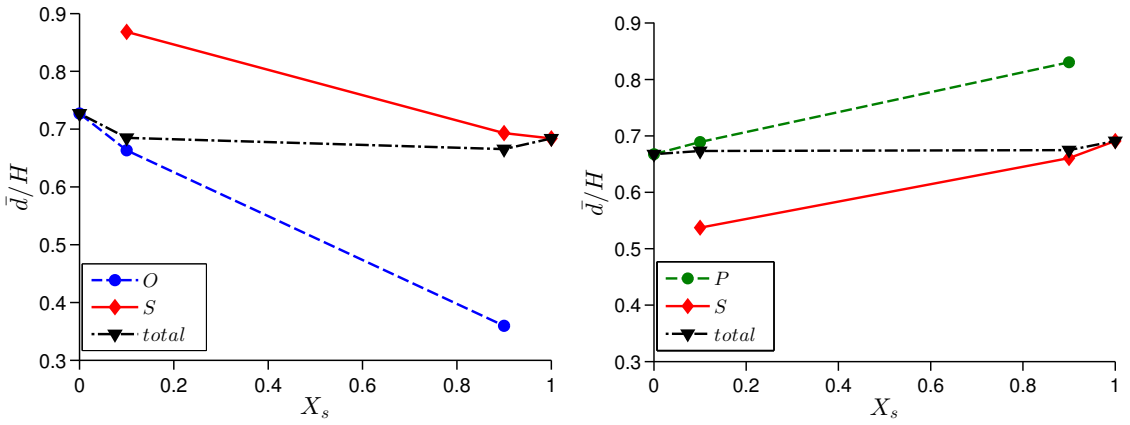

FIG. 4: Steady state $\bar{d}$ as a function of X_s for the mixture of (a) oblate ($\kappa = 0.6$) and spherical, and (b) prolate ($\kappa = 1.33$) and spherical capsules. Also shown is the steady state $\bar{d}$ of the total suspension. Both capsules have same equatorial radius with $\phi_s = 0.10$.

$|\bar{d}_s - \bar{d}_o|$, increases with increase in X_s .

Now we turn to the mixture of prolate and spherical capsules. In Fig. 4(b), we observe that as X_s increases, prolate capsules move toward the center while spherical capsules marginate. The $\bar{d}$ for both species increases with increase in X_s . This is contrary to the behavior of oblate capsules in mixture we saw in earlier paragraph.

To see more detail of the capsule distributions, we now examine the number density of the center of mass of a given species as a function of the y-coordinate normalized by the mean number density n of that species; we denote this as $\hat{n}(y)$. If the distribution were uniform, then this quantity would have a value of one throughout. Note that a subscript 's', 'o' or 'p' may be used in $\hat{n}$ to specifically refer to the spherical, the oblate or the prolate capsules, respectively; the same convention is followed later for denoting other quantities. To compute $\hat{n}(y)$, the channel height is divided into bins and then capsules are assigned to bins based on their center of mass coordinates. The number of capsules in each of the bins is then normalized by the value expected in that bin based on a uniform distribution in the wall normal direction. Temporal averaging of distribution profile is done in the range of $t_s = 2000 - 3000$ using a block averaging technique [57] with blocks of 100 strain units. Block size was selected such that auto-correlation between distribution profiles was less than 5%. Typical error bars are shown in Fig. 11(e).

Fig. 5(a),(b) shows the distribution of capsules in a pure suspension of oblate, spherical or prolate capsules. Two things are immediately clear from these plots. First, there are two peaks, one sharper peak closer to the wall and another broader peak closer to the centerline.

Second, the thickness of the cell-free layer (CFL), the region near the wall with absence of center of mass of capsules, increases with the decrease in κ. A mechanistic explanation for this observation is provided in Sec. IV. The peaks in the $\hat{n}(y)$ profile indicate some layering in the pure suspensions. Similar effects have been seen in the simulation of capsules [5, 7] and drops [58].

Now, we direct our focus to the binary mixtures of capsules of different shapes. Fig. 5(c),(d) shows results for the case where spherical capsules are dilute relative to ellipsoidal ($X_s = 0.1$). In the mixture of oblate and spherical capsules, shown in Fig. 5(c) and Fig. 2(a), we see that spherical capsules demarginate *i.e.* they have higher tendency to be found near centerline, while the oblate capsules are pushed more towards the wall compared to pure suspension, as evidenced in the decrease of the CFL thickness and the higher peak near the wall. In Fig. 5(d) (simulation snapshot in Fig. 3(a)), we examine the mixture of prolate and spherical capsules, spheres being dilute. The CFL thickness for prolate capsules increases compared to the $X_s = 0$ case, indicating that the prolate capsules have moved closer to the center. On the other hand, spherical capsules are observed to marginate: *i.e.* they have higher tendency to be found near the wall.

Next, we examine the case where ellipsoidal (oblate or prolate) capsules are in the dilute regime ($X_s = 0.9$). In a mixture of oblate and spherical capsules (Fig. 5(e) and Fig. 2(b)), the oblate capsules are strongly depleted in the center of channel ($\hat{n}(y) = 0$ near the centerline) and are concentrated near the wall. In the mixture of prolate and spherical capsules, shown in Fig. 5(f) (simulation snapshot in Fig. 3(b)), the prolate capsules strongly demarginate, with the peak concentration near the centerline.

To summarize, the above results indicate that in a mixture of capsules with the same equatorial radius and varying κ, the component with lower/higher κ will marginate/demarginate when present in trace amount. We discuss the mechanistic origin of this observation in Sec. IV.

2. *Effects of aspect ratio and volume fraction*

Now we briefly turn our attention to a more fine-grained examination of the role of κ. Fig. 6(a) shows the distributions at various κ of oblate capsules in a pure suspension ($X_s = 0$) and Fig. 6(b) shows the distribution when the the oblate capsules are dilute ($X_s =$

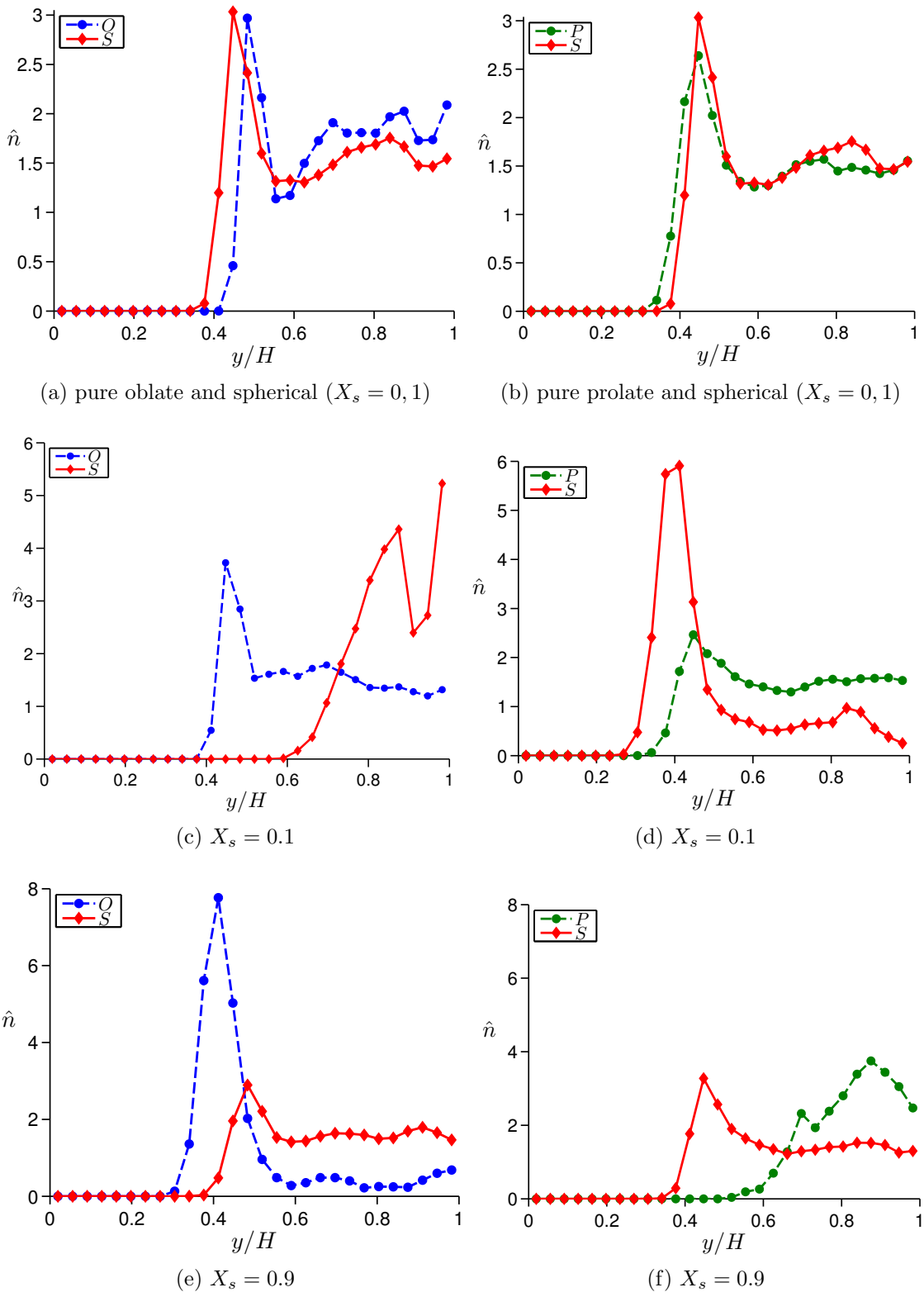

(a) pure oblate and spherical ($X_s = 0, 1$)

(b) pure prolate and spherical ($X_s = 0, 1$)

(c) $X_s = 0.1$

(d) $X_s = 0.1$

(e) $X_s = 0.9$

(f) $X_s = 0.9$

FIG. 5: Normalized number density distributions $\hat{n}(y)$. The channel wall is at $y = 0$ and the centerline at $y = H$. The κ of oblate and prolate capsules is 0.6 and 1.33, respectively with $\phi_s = 0.10$. Both species in the mixture have the same equatorial radius. (a) $X_s = 0$ and $X_s = 1$: Pure species (oblate and spherical capsules), (b) $X_s = 0$ and $X_s = 1$: Pure species (prolate and spherical capsules), (c) $X_s = 0.1$ in oblate-sphere mixture, (d) $X_s = 0.1$ in prolate-sphere mixture, (e) $X_s = 0.9$ in oblate-sphere mixture and (f) $X_s = 0.9$ in prolate-sphere mixture.

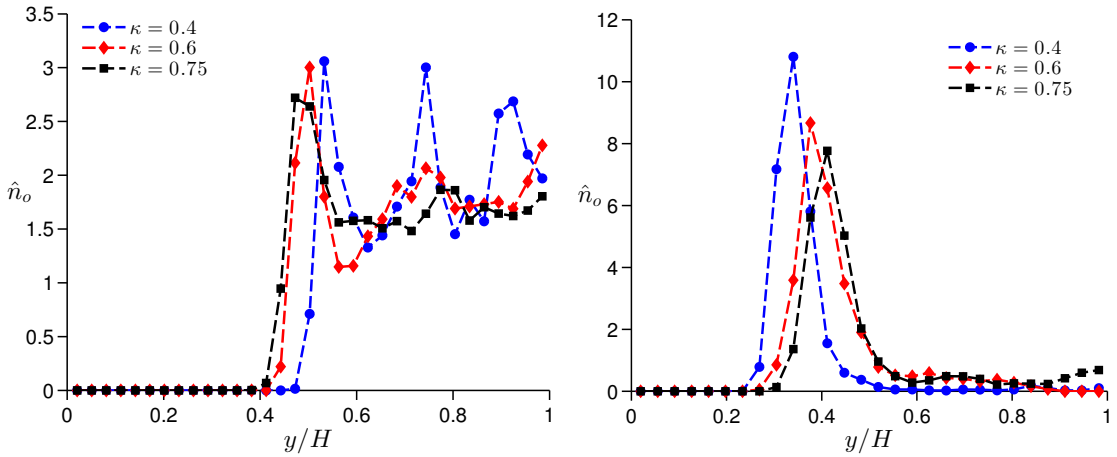

FIG. 6: Normalized number density distribution of oblate capsules $\hat{n}_o(y)$ at several κ for the (a) $X_s = 0$ and (b) $X_s = 0.9$. Both capsules have the same equatorial radius with $\phi_s = 0.10$.

0.9). For pure suspensions, the CFL thickness as well as the peak near wall increases as κ decreases. At the lowest value of κ studied here, $\kappa = 0.4$, we observe multiple peaks in the distribution function indicating multiple layers, however animations reveal that only the peak near the walls is representative of layers, while much of the interior region consists of disorganized particles. As the oblate capsules become the trace component in the mixture, they are increasingly marginated as κ decreases and when $\kappa < 0.6$, we observe complete depletion of oblate capsules from the central region of the channel.

For a suspension of pure spherical capsules, the CFL thickness decreases as ϕ_s increases as seen in the distributions shown in Fig. 7(a). This result is consistent with prior simulations and theory [7, 46, 59, 60]. Also, the near-wall peak diminishes as ϕ_s increases; this occurs in conjunction with a more uniform distribution over the rest of the channel. Fig. 7(b) shows $\hat{n}_s$ for $X_s = 0.9$ in the mixture of spherical and prolate ($\kappa = 1.33$) capsules. Spherical capsules occupy central region of channel at all ϕ_s, while prolate capsules increasingly undergo demargination (not shown). The near-wall peak shifts toward the wall as well as peak-height decreases with increasing ϕ_s, just as in pure suspensions of spherical particles.

B. Volume held constant

Now, we direct our attention to binary mixtures in which all capsules have the same volume V, simulation sets C and D in Table I. As discussed earlier, the equatorial radius a of ellipsoidal capsules will scale as $\kappa^{-1/3}$ in these sets of runs. Thus, oblate and prolate

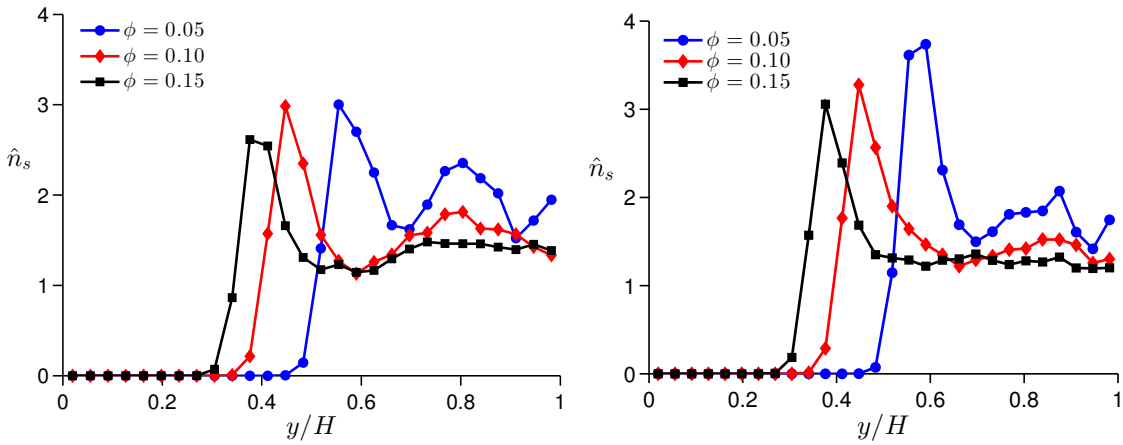

FIG. 7: Normalized number density distribution of spherical capsules $\hat{n}_s(y)$ at several ϕ_s for (a) $X_s = 1$ and (b) $X_s = 0.9$ in a mixture of spherical and prolate ($\kappa = 1.33$) capsules. Both capsules have same equatorial radius.

capsules will have larger and smaller a, respectively, compared to spherical capsules. We first discuss the results for $\kappa = 0.4$ from simulation set C and $\kappa = 2.0$ from simulation set D. Results for varying κ and ϕ are discussed in Sec. III B 2. Fig. 8 and Fig. 9 show representative snapshots (taken at $t = 3000$). It is evident from these snapshots that *both* oblate and prolate capsules demarginate when present in trace amount ($X_s = 0.9$), while spherical capsules marginate when they are trace component ($X_s = 0.1$), in contrast to the behavior we saw earlier in the constant radius case, Sec. III A.

1. *Capsule distributions*

We begin first by presenting in Fig. 10 the mean positions $\bar{d}$ of capsules at several X_s at $\phi = 0.10$. In Fig. 10(a), where $\kappa = 0.4$, $\bar{d}$ for both capsules increases with increasing X_s , with $\bar{d}$ of spherical capsules always staying below that of oblate capsules. Thus spheres marginate when present as the trace component. Notably, this is the opposite of the behavior seen at constant radius (Sec. III A). In simulations of platelet margination, Reasor *et al.* [43] found that spherical platelets marginate more than disk-shaped platelets with the same volume, a tendency seen here as well. (However, their platelets were rigid and all rigid particles marginate strongly in a suspensions of larger flexible ones [48], so it is likely that the effect they observed in more closely related to the dynamics of particles rolling along a vessel wall.) Further insight into this phenomenon is provided in Sec. IV. Fig. 10(b) shows that the prolate capsules (here $\kappa = 2$) demarginate when present as trace, very similar to their

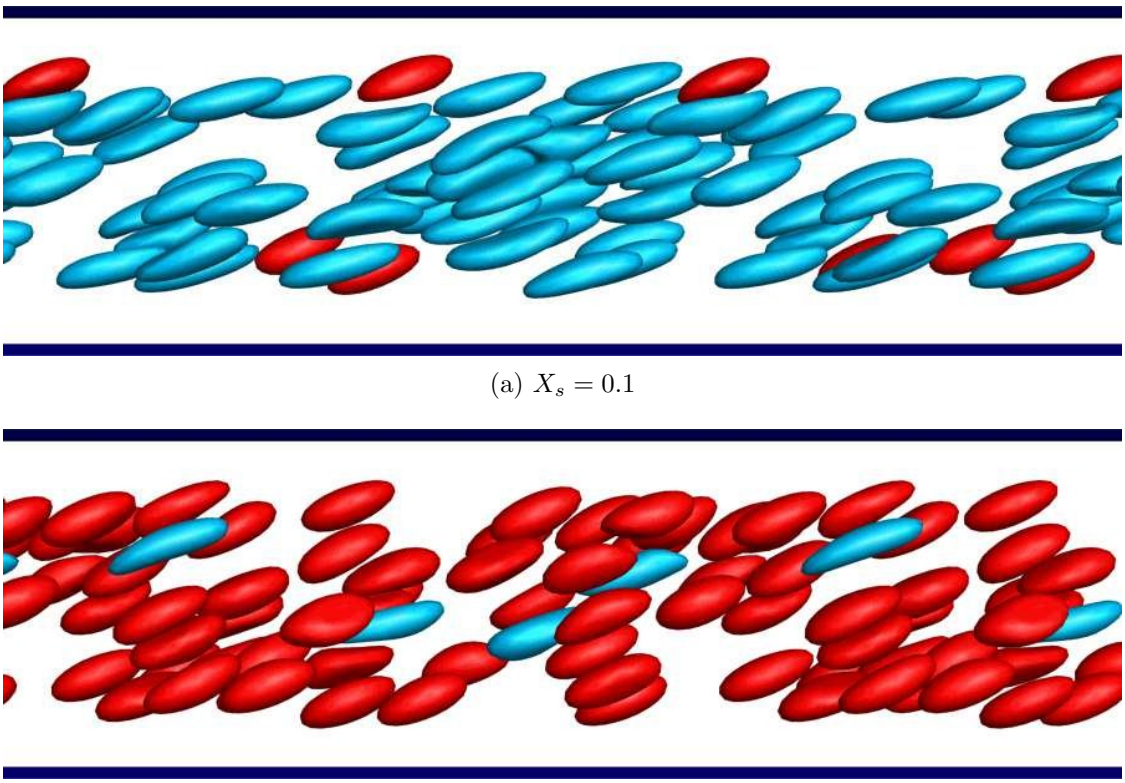

(a) $X_s = 0.1$

(b) $X_s = 0.9$

FIG. 8: Simulation snapshots for mixtures of oblate ($\kappa = 0.4$, blue) and spherical capsules (red) with (a) $X_s = 0.1$ and (b) $X_s = 0.9$. Both species have same volume with $\phi = 0.10$.

behavior seen in the constant-radius case.

Fig. 11 shows number density profiles $\hat{n}(y)$ at various X_s . The result for pure suspensions is shown in Fig. 11(a,b), where two things can be noticed immediately: a) the cell-free layer thickness l_d is the same for all three capsule shapes and b) the near wall peak for spherical capsules is bigger than ellipsoidal capsules. A mechanistic explanation of these observations presented in Sec. IV.

Next, we focus on mixtures. In Fig. 11(c,d), we present the case where spherical capsules are in trace amount ($X_s = 0.1$). In the case of oblate and spherical capsules, shown in Fig. 11(c) and Fig. 8(a), we see that oblate capsules occupy the region close to centerline while the spherical capsules marginate. Prolate capsules are seen to have similar behavior in Fig. 11(d) and Fig. 9(a). For the case where spherical capsules are primary ($X_s = 0.9$), shown in Fig. 11(e,f)(snapshot in Fig. 8(b) and Fig. 9(b)) for oblate and prolate capsules, respectively, the ellipsoidal capsules demarginate when they are present in trace amount. We provide a mechanistic explanation for these trends in Sec.IV.

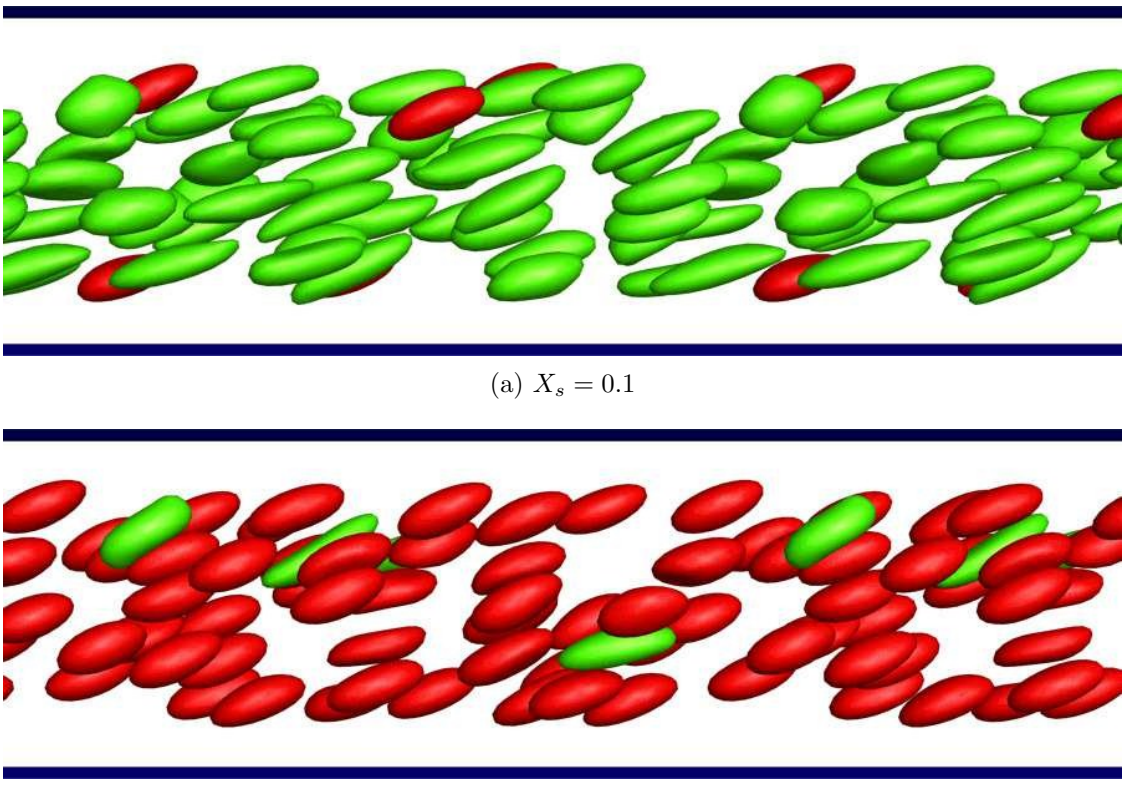

(a) $X_s = 0.1$

(b) $X_s = 0.9$

FIG. 9: Simulation snapshots for mixtures of prolate ($\kappa = 2.0$, blue) and spherical (red) capsules with (a) $X_s = 0.1$ and (b) $X_s = 0.9$. Both species have same volume with $\phi = 0.10$.

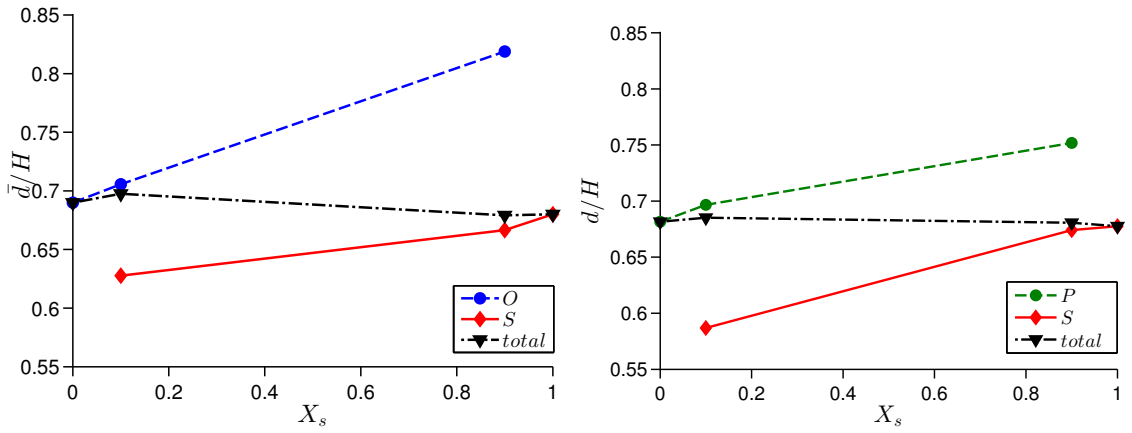

FIG. 10: Steady state $\bar{d}$ as a function of X_s for the mixture of (a) oblate ($\kappa = 0.4$) and spherical capsules and (b) prolate ($\kappa = 2$) and spherical. Also shown is the steady state $\langle\bar{d}\rangle$ of the total suspension. Both capsules have same volume and $\phi = 0.10$.

2. *Effects of aspect ratio and volume fraction*

Now, we turn our attention to the effect of κ, while keeping the other parameters fixed. Fig. 12(a) shows the distribution of prolate capsules in wall-normal direction for a pure

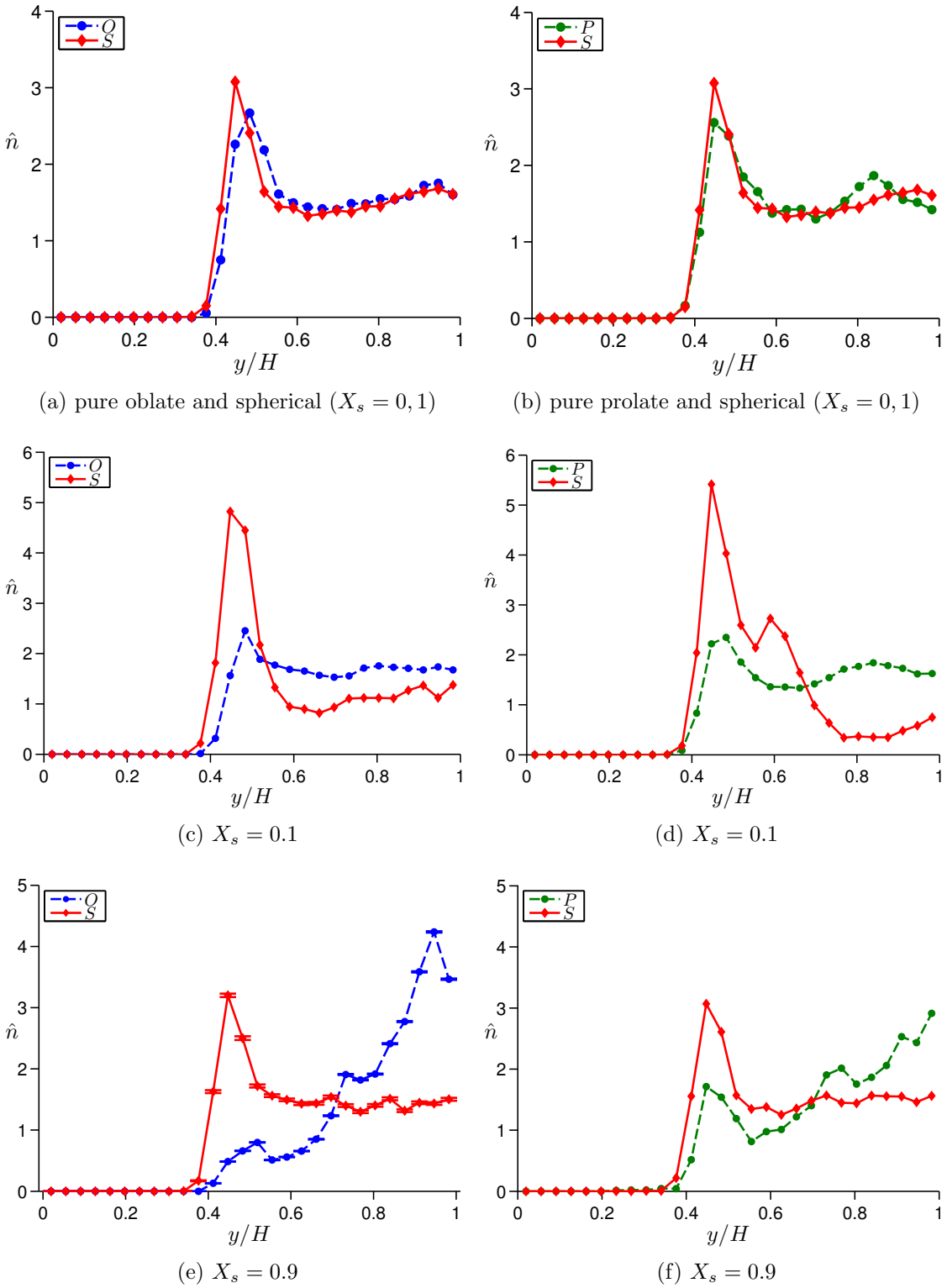

(a) pure oblate and spherical ($X_s = 0, 1$)

(b) pure prolate and spherical ($X_s = 0, 1$)

(c) $X_s = 0.1$

(d) $X_s = 0.1$

(e) $X_s = 0.9$

(f) $X_s = 0.9$

FIG. 11: Normalized number density distributions $\hat{n}(y)$ for suspensions whose components have the same volume. The aspect ratios κ of the oblate and prolate capsules are 0.4 and 2.0, respectively with $\phi = 0.10$. (a) $X_s = 0$ and $X_s = 1$: Pure species (oblate and spherical capsules), (b) $X_s = 0$ and $X_s = 1$: Pure species (prolate and spherical capsules), (c) $X_s = 0.1$ in oblate-sphere mixture, (d) $X_s = 0.1$ in prolate-sphere mixture, (e) $X_s = 0.9$ in oblate-sphere mixture and (f) $X_s = 0.9$ in prolate-sphere mixture.

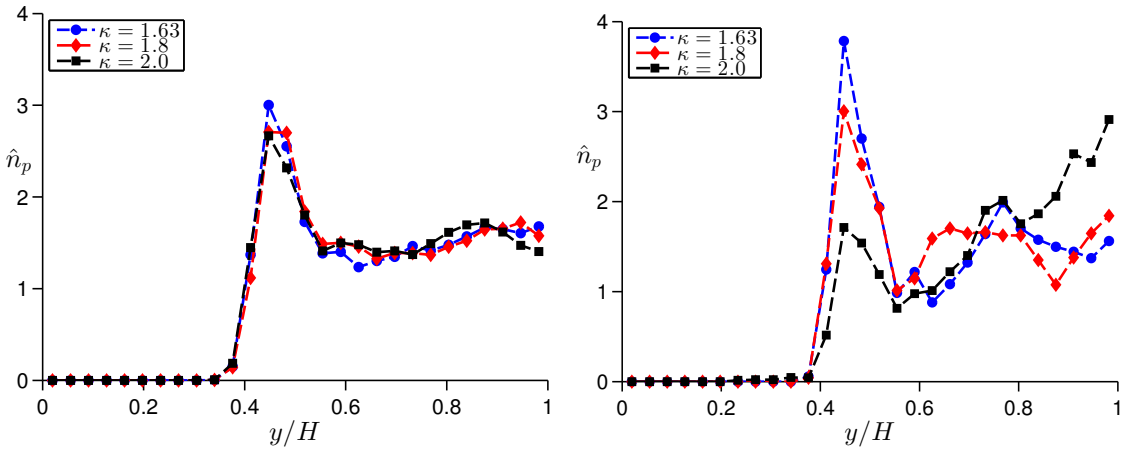

FIG. 12: Number density distribution of prolate capsules $\hat{n}_p(y)$ at several κ for the (a) $X_s = 0$ and (b) $X_s = 0.9$ (prolate-sphere mixture). Both species have same volume with $\phi = 0.10$.

suspension ($X_s = 0$) and Fig. 12(b) shows the distribution when they are present in the trace limit ($X_s = 0.9$) at varying κ. For pure suspensions, we see that the CFL thickness as well as the near-wall peak is the same for all three different κ ($\kappa = 1.63, 1.8, 2$). As the prolate capsules become dilute, their near-wall peak decreases while their concentration at the centerline increases (increasing demargination) with increasing κ.

To examine the effect of volume fraction, we present results for mixture of oblate ($\kappa = 0.4$) and spherical capsules at $X_s = 0.9$ in Fig. 13. Normalized number density distribution of oblate and spherical capsules is shown in Fig. 13(a) and (b), respectively. Oblate capsules demarginates at all ϕ and are increasingly found near center of the channel as ϕ increase. While for spherical capsules, the near-wall peak shifts toward the wall with increasing ϕ, just as in pure suspensions of spherical particles (Fig. 7(a)), indicating that they are increasingly pushed towards wall with increase in ϕ.

C. Effect of domain size

In order to ensure that the results presented above were generated in a large enough simulation domain in the periodic directions, we conducted additional runs for a mixture of oblate ($\kappa = 0.75$) and spherical capsules with the same equatorial radius a at $\phi_s = 0.10$ in a simulation domain of $20.31a_s \times 20.31a_s \times 10.155a_s$ (with 96 capsules). Comparative results for component distributions at $X_s = 0.9$ are shown in Fig. 14 and we note that the differences are small.

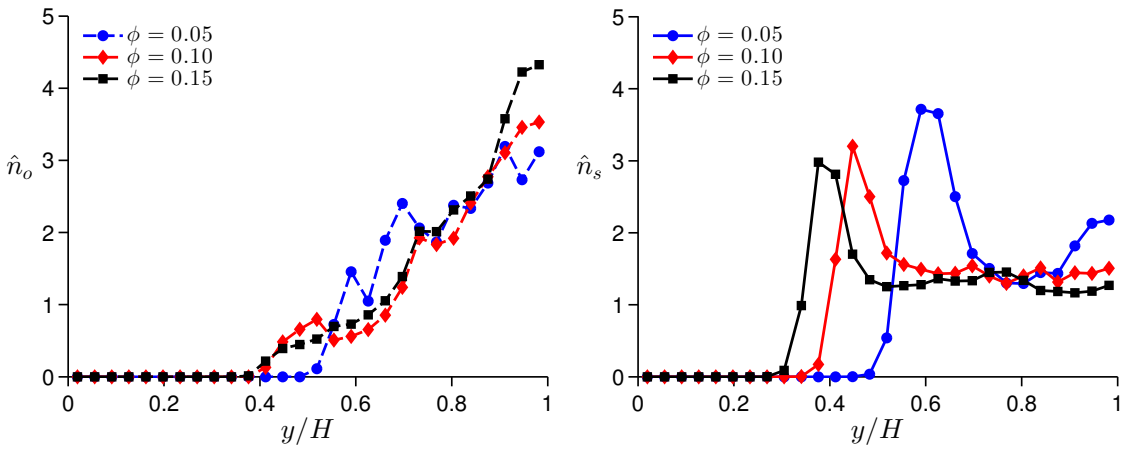

FIG. 13: Normalized number density distribution $\hat{n}(y)$ of (a) oblate and (b) spherical capsules at several ϕ for $X_s = 0.9$ in a mixture of spherical and oblate ($\kappa = 0.4$) capsules. Both species have the same volume.

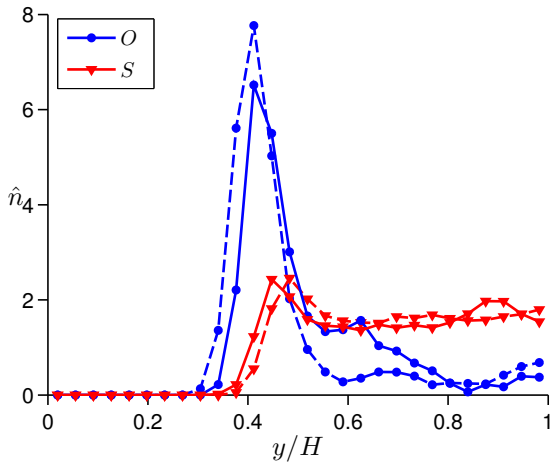

FIG. 14: Normalized number density distribution of components $\hat{n}(y)$ at $X_s = 0.9$, $\phi_s = 0.10$ in the mixture of oblate ($\kappa = 0.75$, shown in blue closed circles) and spherical (shown in red closed triangles) capsules with same equatorial radius. Results are shown for two different box size: $20.31a_s \times 10.155a_s \times 10.155a_s$ (with 48 capsules, shown with solid curve) and $20.31a_s \times 20.31a_s \times 10.155a_s$ (with 96 capsules, shown with dashed curve).

IV. MECHANISMS AND SIMPLIFIED MODEL

Above we presented detailed results for capsules having different shapes while maintaining (a) same equatorial radius, and (b) same volume. On the surface, the results for these two cases suggest contradictory trends. In this section, however, we show that the mechanistic origins of binary suspension dynamics in both cases can be understood within the same framework: as a competition between two key processes, (a) wall-induced migration, which tries to push capsules toward the center of channel, and (b) shear-induced collisions, which try to homogenize the capsule distribution.

A. Wall-induced migration

In general, a suspended deformable object such as a drop, capsule, cell or flexible polymer molecule subjected to shear flow near a no-slip wall will migrate normal to the wall even in the Stokes flow limit [61, 62]. We have computed this migration velocity $v_m(y)$ for isolated capsules in a slit domain of sized $10.155a_s \times 10.155a_s \times 10.155a_s$. Again in all cases $\mathrm{Ca} = 0.5$. The simulation to compute v_m at a given wall-normal position y begins by placing the initially spherical capsule at that location. With time, the shape of the capsule as well as the location of its center of mass evolves. We find the quasi-steady limit of the migration velocity by holding the center of mass of the capsule fixed at a given location: at the end of each time step, the capsule is translated so that its center of mass returns to its original position; at steady state this displacement and the time step determine the quasi-steady migration velocity. In general, the time scale of capsule shape evolution is much faster than that of capsule motion in the wall-normal direction. As a result, except in the near-wall region of the standard simulation (see [52]), the migration velocity obtained from the above described scheme is very close to that from a standard simulation.

Fig. 15(a) shows $v_m(y)$ for capsules with the same equatorial radius and varying κ at confinement ratio of $C = 5.08$. We observe that $v_m(y)$ increases with increasing κ; recall that capsules with same equatorial radius have increasing volume as κ increases. Fig. 15(b) shows $v_m(y)$ of capsules of the same volume and varying κ. Perhaps surprisingly, in this case there is almost no change in v_m with κ.

The trends shown in Fig. 15 clearly indicate that the volume of capsule plays a larger role in determining migration velocity than its shape. Further insights into these results can be gained from some theoretical considerations. To leading order far from walls a deformable neutrally buoyant object in fluid can be treated as a symmetric force-dipole characterized by the stresslet tensor $\mathbf{S}$ [61, 62]. In a semi-infinite domain with a no-slip wall at $y = 0$ the migration velocity induced by the image of this dipole in the wall can be approximated as:

$$v_m = \frac{K_m}{y^2}, \tag{6a}$$

$$K_m = -\frac{9S_{yy}}{64\pi\mu}. \tag{6b}$$

For a spherical capsule in the limit of small Ca, Barthes-Biesel and Chhim [63] gave the

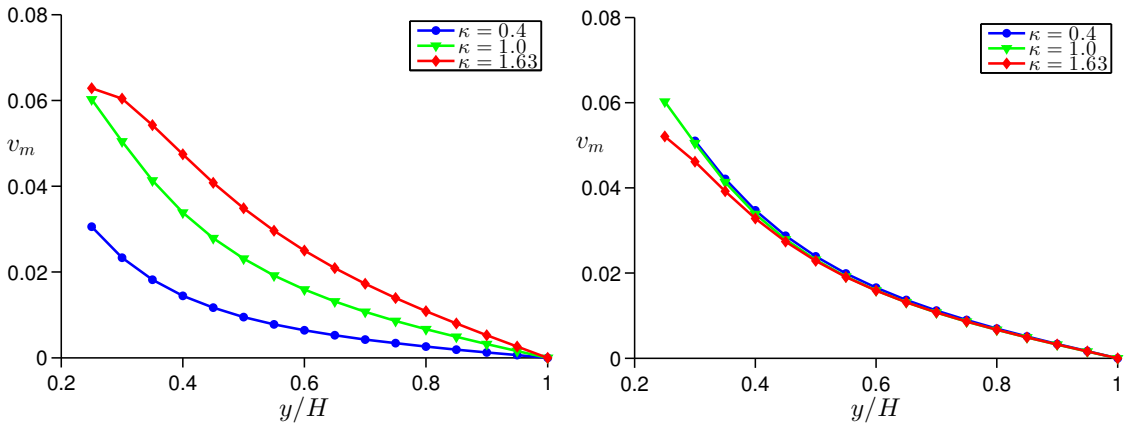

FIG. 15: Migration velocity of a single capsule for varying κ with (a) same equatorial radius and (b) same volume.

following expression for the yy component of the stresslet:

$$S_{yy} \sim -\mu\dot{\gamma}V\mathrm{Ca}. \tag{7}$$

Thus at constant Ca, the migration velocity is linearly proportional to its volume. Based on our observations, we suggest that this dependence holds, at least to a very good approximation, for nonspherical capsules. This argument can be recast using dimensional analysis. For a capsule with spherical rest shape in the point dipole limit,

$$\frac{v_m}{\dot{\gamma}a} \sim \frac{a^2}{y^2} f(\mathrm{Ca}) \tag{8}$$

or equivalently

$$v_m \sim \frac{\dot{\gamma}V}{y^2} f(\mathrm{Ca}), \tag{9}$$

since $V \sim a^3$. For a nonspherical capsule the additional dimensionless group κ appears and the above result directly generalizes to

$$v_m \sim \frac{\dot{\gamma}V}{y^2} f(\mathrm{Ca}, \kappa). \tag{10}$$

Our results indicate that at least for the model under consideration here $f(\mathrm{Ca}, \kappa)$ is a very weak function of κ.

B. Pair collisions

In a dilute suspension of capsules, the capsule-capsule interactions can be treated as a sequence of uncorrelated pair collisions [7, 47, 48, 64]. The probability of three-body or higher interactions is at least an $O(\phi)$ smaller. Evidently, pair collisions will play an important part in capsule transport. In a binary mixture two types of collisions will occur: (a) homogeneous collisions where capsules of same type collide, and (b) heterogeneous collisions where capsules of different type collide. Fig. 16 shows a schematic for the heterogeneous pair collisions.

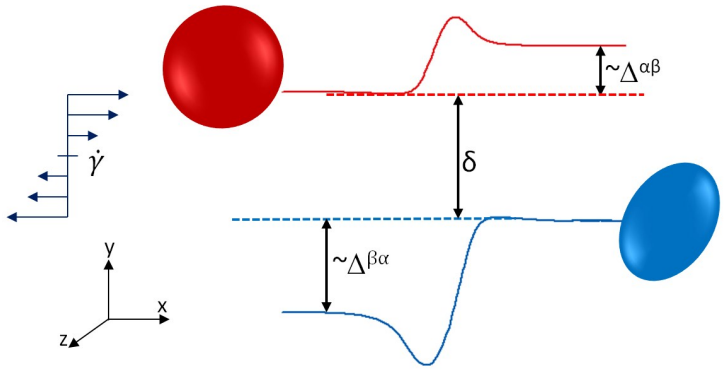

FIG. 16: Schematic of capsule trajectories in a pair collision. Here α and β refer to the species types of the two colliding capsules, δ_y is the pre-collision offset in the gradient direction, and $\Delta^{\alpha\beta}$ and $\Delta^{\beta\alpha}$ are the cross-stream displacements of the capsules α and β, respectively.

To examine the dependence of these collisions on aspect ratio and volumes, pair collision simulations were performed in an effectively unconfined domain with side $30a_s$ in each direction. Capsules of different shapes were initially placed symmetrically on either side of the centerline with their equatorial plane parallel to the flow direction. The capsules have a pre-collision offset of δ_y in the gradient direction, δ_z in the vorticity direction and $8a$ in the flow direction (see Fig. 16). In this section, we will present result for pair-collisions where $\delta_z = 0$. The trajectories of capsules in homogeneous and heterogeneous pair collisions between sphere and oblate ellipsoid ($\kappa = 0.4$, same a) for one such case with $\delta_y = 0.5$ is shown in Fig. 17. For this case, the final cross-stream displacement of the sphere (Δ^{ss}) is higher than that of the ellipsoid (Δ^{oo}) in their respective homogeneous pair-collision. In a heterogeneous pair collision, the oblate capsule displaces more than the sphere ($\Delta^{os} > \Delta^{so}$). This differential displacement has important consequences for the segregation.

Moving from this specific case, the steady-state cross-stream displacements Δ of capsules as a function κ is reported in Fig. 18. We begin discussion with the result for pair collisions

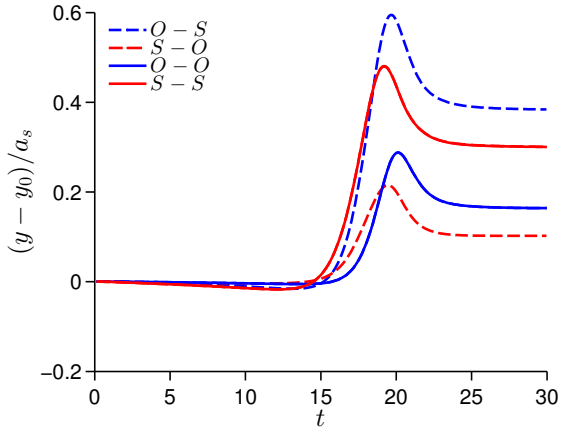

FIG. 17: Relative trajectories for spherical ('S') and oblate ('O') with $\kappa = 0.6$ and same a in both homogeneous ($S-S$, $O-O$) and heterogeneous ($S-O$, $O-S$) pair collisions. y_0 is the initial position in y direction of a capsule.

of capsules with the same a, shown in Fig. 18(a). In all cases, we studied the pair collision of a spherical capsule with an ellipsoidal (either oblate or prolate) capsule. The solid curve shows Δ for homogeneous collision of ellipsoidal capsules, while the dashed curves show $\Delta^{\alpha\beta}$ of each capsule in a heterogeneous collision. The curves meet at $\kappa = 1$, the case of homogeneous collision of spheres. Notice that the cross-stream displacement of an oblate capsule is larger than for a spherical capsule in heterogeneous collision, so $\Delta^{os} > \Delta^{so}$, while for homogeneous collision, $\Delta^{oo} < \Delta^{ss}$. In general, the order of displacement is as follows: $\Delta^{so} < \Delta^{oo} < \Delta^{ss} < \Delta^{os}$. An obvious trend emerges here: the capsule of high κ gets displaced less in heterogeneous collision compared to their homogeneous collision while displaces low κ capsule more in heterogeneous collision compared to their homogeneous collision. This trend continues for the pair collision of spherical and prolate capsules as well where we observe the following order: $\Delta^{ps} < \Delta^{ss} < \Delta^{pp} < \Delta^{sp}$.

In Fig. 18(b) we turn to the constant volume case. Here as well, the solid curve shows Δ for homogeneous collision of ellipsoidal capsules, while the dashed curves show the $\Delta^{\alpha\beta}$ of each capsule in a heterogeneous collision. In this case, all the curves are nonmonotonic. We can divide the plot into three regions: a) $\kappa < 0.5$: here, $\Delta^{os} < \Delta^{oo} < \Delta^{ss} < \Delta^{so}$, b) $0.5 < \kappa < 1.3$: in this region $\Delta^{\alpha\alpha}$ and $\Delta^{\alpha\beta}$ are nonlinear and close to each other, and c) $\kappa > 1.3$: in this region, where $\Delta^{ps} < \Delta^{pp} < \Delta^{ss} < \Delta^{sp}$.

If we put the results discussed in previous sections Sec. IV A and IV B together, a clearer picture of segregation starts to emerge. The question we ask ourselves here is whether a capsule stuck in near-wall region be able to escape to central region. We focus discussion on the case of oblate and spherical capsule mixture, where both species have same radius.

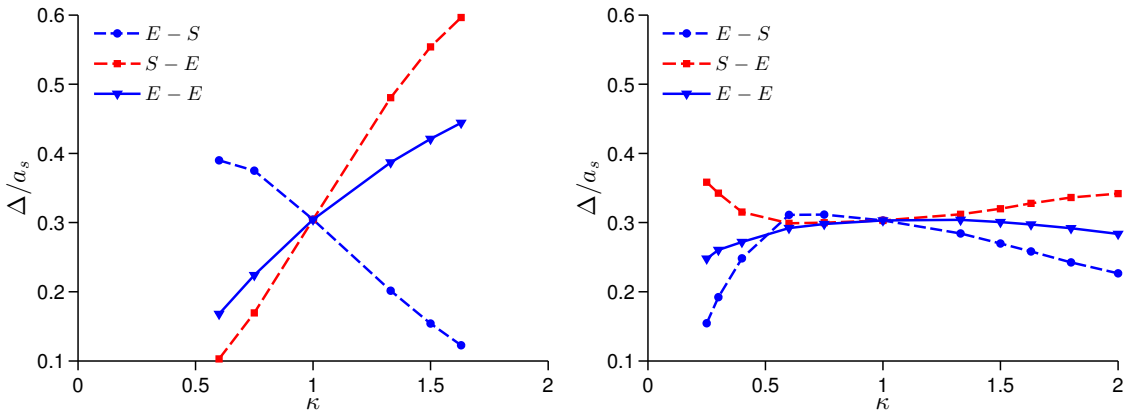

FIG. 18: Post collisional cross-stream displacements of ellipsoidal ('E') and spherical ('S') capsules in homogeneous and heterogeneous collisions as a function of κ for (a) capsules with same equatorial radius and (b) same volume. Other parameters: $\delta_y = 0.5$, $\delta_z = 0$ and $C = 15$.

Consider two scenarios: a) when a slow migrating capsule (here oblate) is in near-wall region surrounded by fast migrating capsule (here sphere); case of $X_s = 0.9$. In subsequent collisions, capsule which displaces less in collision (here sphere) will push other capsule which displaces more (here oblate) towards the wall. As oblate is migrating slowly and is pushed more, it will marginate. In scenario b) a fast migrating capsule (here sphere) is in near-wall region surrounded by slow migrating capsule (here oblate); case of $X_s = 0.1$. In subsequent collisions, less displacing capsule in collision (here sphere) will push more displacing capsule (here oblate) away, making its way to central region. As sphere is migrating faster and displacing less, it will demarginate.

Using the above framework, we can similarly explain the demargination of prolate capsules seen in mixture of prolate and sphere with same radius in Sec. III A. For capsules of same volume, they have similar v_m as seen in Sec. IV A. In such cases, segregation will be driven by heterogeneous collisions. Using above framework, we can deduce that a less displacing capsule in collision will push the capsule which displaces more towards wall. For ellipsoidal ('e') and spherical ('s') capsules, $\Delta^{es} < \Delta^{se}$, thus above framework predicts that both oblate and prolate will demarginate when present in dilute limit (case of $X_s = 0.9$) and sphere will marginate when present in dilute limit (case of $X_s = 0.1$), which indeed is the case as seen in results presented in Sec. III B.

V. KINETIC DRIFT-DIFFUSION THEORY

In recent work, Henríquez *et al.* [48] gave a mathematical model for predicting flow-induced segregation that formalizes earlier mechanistic arguments by Kumar and Graham [45]. In this section we present aspects of this theory and apply it to the shape segregation problem. Consider a dilute suspension ($\phi \ll 1$) containing N_s types of deformable capsules undergoing simple shear flow in a slit. Quantities referring to a specific component α in the mixture will have subscript α: for example n_α is the number density of component α. Consistent with the diluteness assumption, the shear rate $\dot{\gamma}$ is assumed to be independent of the local number densities and thus independent of position. In a dilute suspension the capsule-capsule interactions can be treated as a sequence of uncorrelated pair collisions [47, 58, 64]. The contributions of three-body or higher interactions is $O(\phi^3)$ and is neglected here. Since the capsules are deformable, they migrate away from the wall during flow with velocity $v_{\alpha m}(y)$ as described above. The evolution of the capsule number density distributions can be idealized by a kinetic master equation that captures both the migration and collision effects ([6, 7, 46, 47]). Assuming uniform capsule distributions in x and z, this equation is

$$\frac{\partial n_\alpha(y,t)}{\partial t} = -\frac{\partial}{\partial y}\big(v_{\alpha m}(y) n_\alpha(y,t)\big) + \sum_{\beta=1}^{N_s}\left(\int_{-(2H-y)}^{y}\int_{-\infty}^{\infty}\Big\{n_\alpha(y-\Delta_y^{\alpha\beta}, z-\Delta_z^{\alpha\beta}, t) \times n_\beta(y-\Delta_y^{\alpha\beta}-\delta_y, z-\Delta_z^{\alpha\beta}-\delta_z, t) - n_\alpha(y,z,t) n_\beta(y-\delta_y, z-\delta_z, t)\Big\}\dot{\gamma}\,|\delta_y|\,d\delta_z d\delta_y\right). \quad (11)$$

The term $\dot{\gamma}|\delta_y|$ in the integrand accounts for the relative velocity of approach of two capsules separated far upstream by a wall-normal offset δ_y. In the important special case of a binary suspension composed of a "primary" component ($\alpha =$'p') and a "trace" component ($\alpha =$'t'), such that $n_p \gg n_t$, only the term corresponding to $\beta =$'p' contributes to the sum – the trace component is too dilute for its collisions to affect the behavior of the system. This is the case we consider here.

Under the further conditions: (a) small collisional displacements *i.e.* $\Delta_y^{\alpha\beta}/a \ll 1$, (b) $\Delta_y^{\alpha\beta}$ are vanishingly small for large $|\delta_y|$, and (c) terms involving $(\Delta^{\alpha\beta})^3$ and smaller are negligible, one can approximate the master equation by the following pair of drift-diffusion

type equations [48]:

$$\frac{\partial n_p}{\partial t} = -\frac{\partial}{\partial y}\left[K_{pm}\left(\frac{1}{y^2} - \frac{1}{(2H-y)^2}\right)n_p - K_{pc}\frac{\partial \dot{\gamma} n_p}{\partial y}n_p - \frac{\partial}{\partial y}\left(K_{pd}\dot{\gamma}n_p^2\right)\right],$$
$$\frac{\partial n_t}{\partial t} = -\frac{\partial}{\partial y}\left[K_{tm}\left(\frac{1}{y^2} - \frac{1}{(2H-y)^2}\right)n_t - K_{tc}\frac{\partial \dot{\gamma} n_p}{\partial y}n_t - \frac{\partial}{\partial y}\left(K_{td}\dot{\gamma}n_p n_t\right)\right]. \quad (12)$$

We denote this as the simplified drift-diffusion (SDD) model. Notice that the primary component dominates the collisional drift velocity (second term in RHS) and collisional-diffusivity (third term in RHS) terms. Here, $K_{\alpha m}$, $K_{\alpha c}$ and $K_{\alpha d}$ are migration, collisional drift and collisional diffusivity coefficients, respectively, of capsules of type α, defined as:

$$v_m^{\alpha} = K_{\alpha m}\left[\frac{1}{y^2} - \frac{1}{(2H-y)^2}\right], \quad (13a)$$
$$K_{\alpha c} = 2\int_0^{r_{cut}} \widehat{\Delta_y^{\alpha p}}(\delta_y)\delta_y|\delta_y|\, d\delta_y, \quad (13b)$$
$$K_{\alpha d} = \int_0^{r_{cut}} \widehat{(\Delta_y^{\alpha p})^2}(\delta_y)|\delta_y|\, d\delta_y, \quad (13c)$$
$$\widehat{\Delta_y^{\alpha p}}(\delta_y) = \int_{-r_{cut}}^{r_{cut}} \Delta_y^{\alpha p}(\delta_y, \delta_z)d\delta_z, \quad (13d)$$
$$\widehat{(\Delta_y^{\alpha p})^2}(\delta_y) = \int_{-r_{cut}}^{r_{cut}} \{\Delta_y^{\alpha p}(\delta_y, \delta_z)\}^2 d\delta_z. \quad (13e)$$

In Eq. 13, r_{cut} is the radius beyond which capsule-capsule interaction is assumed to be negligible. An important feature of Eq. 12 is that steady state solutions with no-flux boundary conditions at wall ($y = 0$) and centerline ($y = H$) can be solved analytically. Number density distributions n_p and n_t are found to be:

$$n_p = \begin{cases} 0, & y < l_d \\ n_{pc}\left(1 - \frac{\left(\frac{H-y}{H-l_d}\right)^2}{\left(\frac{y}{l_d}\right)\left(\frac{2H-y}{2H-l_d}\right)}\right), & y > l_d \end{cases}, \quad (14)$$

$$n_t = \begin{cases} 0, & y < l_d \\ n_{tc}\left(\frac{n_p(y)}{n_{pc}}\right)^M, & y > l_d \end{cases}, \quad (15)$$

Here, n_{pc} and n_{tc} are the number density of primary and trace component at centerline,

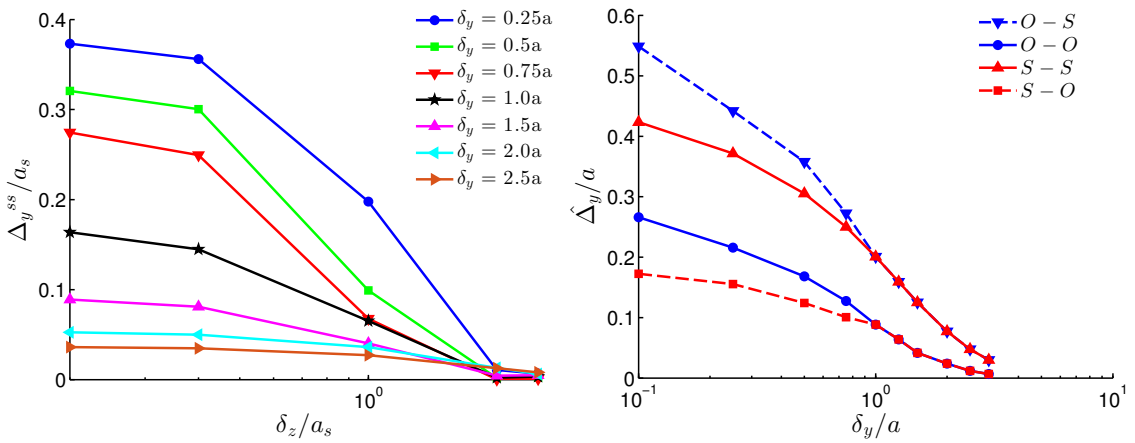

FIG. 19: (a) Post-collisional cross-stream displacement Δ_y^{ss} of spherical capsules in homogeneous collision as a function of δ_z and (b) z-averaged post collisional cross-stream displacement (using Eq. 13(d)) $\widehat{\Delta_y^{\alpha\beta}}(\delta_y)$ as a function of δ_y for pair-collisions between oblate ($\kappa = 0.4$) and spherical capsule.

respectively, l_d is the cell-free layer thickness

$$l_d = C\left(1 - \sqrt{\frac{C\phi_{pc}}{2\eta_p + C\phi_{pc}}}\right), \tag{16}$$

where $\eta_p = \kappa_m/(\kappa_c + 2\kappa_d)$ is the ratio of nondimensional migration coefficient over collisional coefficients and M is the so-called *margination parameter*,

$$M = \frac{K_{pc} + K_{pd}}{K_{td}}\left(\frac{K_{tm}}{K_{pm}} - \frac{K_{tc} + K_{td}}{K_{pc} + 2K_{pd}}\right). \tag{17}$$

This dimensionless group captures the competition between the migration velocities of two component and their collisional terms. The qualitative nature of the concentration profile of trace component is determined by M. Four distinct regimes can be identified: a) $M > 1$: trace component demarginates, b) $0 < M < 1$: trace component weakly marginates, c) $-1 < M < 0$: trace component moderately marginates, and d) $M \leq -1$: trace component strongly marginates. In this last case there is no steady solution for $n_t(y)$: initial conditions evolve to a delta-function localized at $y = l_d$, i.e. at the edge of the cell-free layer.

We will evaluate the predictions of this theory for a suspension where ellipsoidal capsules are the trace component, specifically the $X_s = 0.9$ case described above. To do this, the migration velocities v_m^α must be computed as well as the collision integrals, Eq. 13, which require knowledge of the cross-stream displacements $\Delta^{\alpha\beta}$ in pair collisions. These were

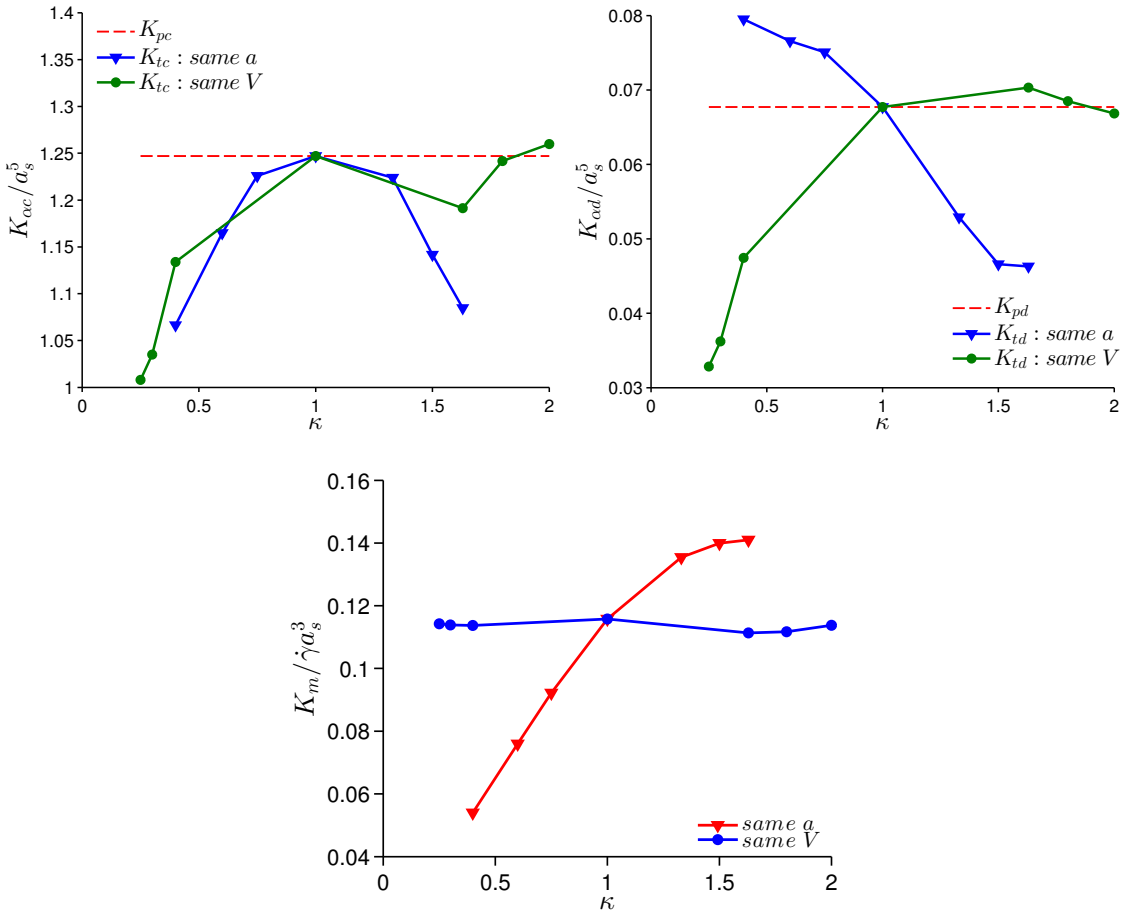

FIG. 20: (a) Collisional drift coefficient $K_{\alpha c}$, (b) collisional diffusion coefficient $K_{\alpha d}$ and (c) migration coefficient $K_{\alpha m}$ as a function of κ for cases where capsule have same a and same V.

determined as described in the previous section. Pair collisions were studied with several δ_y and δ_z for a capsule pair; these were varied in the range $[0.1a, 2.5a]$ and $[0.1a, 2.5a]$ for each of the κ studied in table I. Fig. 19(a) shows results for homogeneous pair collisions while Fig. 19(b) shows results for heterogeneous collision between oblate spheroids of $\kappa = 0.4$ and spheres, where both capsules have same a. Observe that Δ_y decays rapidly with δ_y and δ_z. The trends of Δ_y in Fig. 19(b) affirm the results shown earlier in Fig. 18. Similarly, to compute wall-induced migration velocities $v_m^{\alpha}(y)$, simulations were performed for all κ listed in table I.

Using the displacement functions $\Delta^{\alpha\beta}(\delta_y, \delta_z)$, the integrals to compute $K_{\alpha c}$ and $K_{\alpha d}$ were done using the trapezoid rule. In this work, r_{cut} is kept at $2.5a$ based on results shown in Fig. 19. Fig. 20(a) shows the K_{tc}, Fig. 20(b) shows K_{td} and 20(c) shows K_{tm} for the cases (a) capsules with same a and (b) capsules with same V. Values of K_{pc}, K_{pd} and K_{pm} are given by these results evaluated at $\kappa = 1$. Trends in these parameters are all consistent with

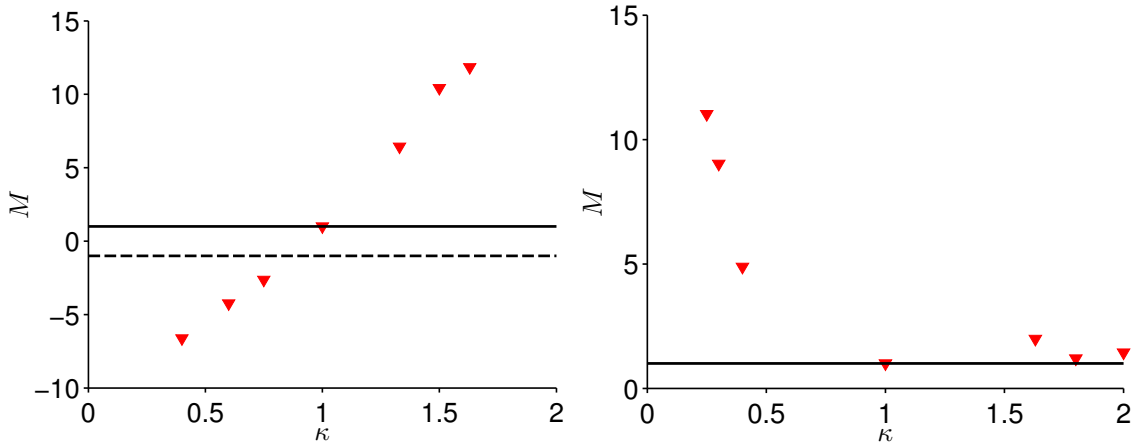

FIG. 21: Margination parameter M as a function of κ for (a) capsules with same equatorial radius and (b) same volume. The region above the solid line ($M = 1$) is the demargination regime, while the region below the dashed curve ($M = -1$) is the strong margination (drainage) regime.

the trends on the displacements and migration velocities described above.

With these coefficients in hand, the margination parameter M can be computed using Eq. 17. Fig. 21 shows M as a function of κ for the case of (a) same a and (b) same V. Fig. 21(a) shows that for oblate capsules, $M < -1$ for all three values of κ studied in Sec. III A. The SDD theory thus predicts strong margination of the oblate capsules. We indeed see this in the simulation results of Sec. III A. For prolate capsules, $M > 1$ for all three κ values studied in Sec. III A. In this case, theory predicts demargination of trace component which is indeed seen in the simulation results of Sec. III A. For the case when the ellipsoidal capsules have the same V as the spherical, we see that $M > 1$ for all values of κ. In this case, the theoretical prediction is that both oblate and prolate will demarginate; this is also found in the simulations in Sec. III B.

One can also calculate the theoretical number density profile of the trace component with the knowledge of M using Eq. 15. Fig. 22 shows the centerline normalized number density $\hat{n}_{tc}$ of trace component as a function of M. Very good agreement between simulations and theory is found.

The SDD theory also predicts the thickness of cell-free layer l_d (Eq. 16). This prediction and the simulation results as a function of overall volume fraction ϕ are shown in Fig. 23 for (a) same a, and (b) same V. In Eq. 16, the normalized centerline volume fractions from their pure suspension runs were used. With increase in ϕ, l_d decreases for all three species in their pure suspension as seen both in simulation and theory. Furthermore, for the same a at a

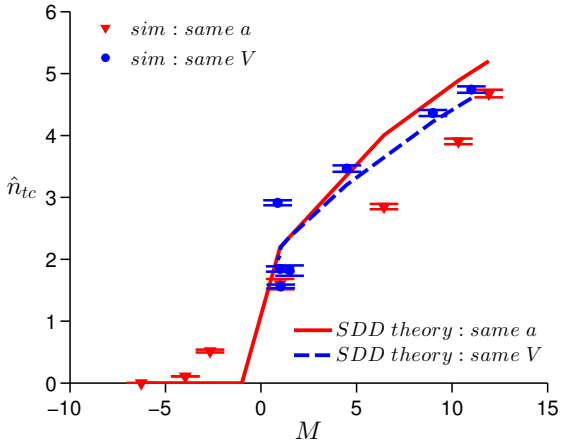

FIG. 22: Normalized number density of trace component at the center of channel versus margination parameter. Solid lines are theoretical prediction while the symbols are taken from full boundary integral simulation presented earlier in Sec. III for $\phi_s = 0.10$.

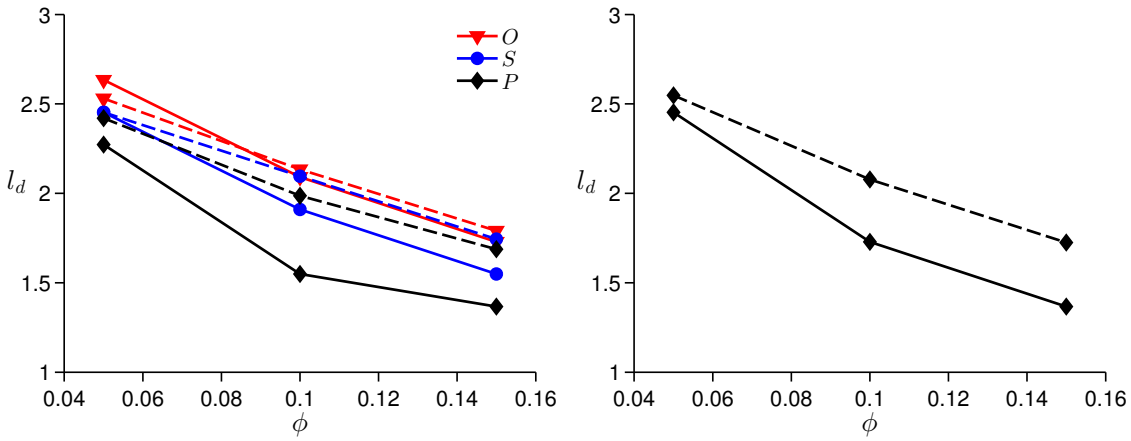

FIG. 23: Cell-free layer thickness obtained from SDD theory (dashed curve) and simulation (solid curve) as a function of total volume fraction for (a) capsules with same a ($\kappa = 0.6$ for 'O' and $\kappa = 1.33$ for 'P') and (b) capsules with same V ($\kappa = 0.4$ for 'O' and $\kappa = 1.8$ for 'P').

particular ϕ, $l_d^o > l_d^s > l_d^p$: this trend is seen for both simulation and theory and is a reflection of the trend of $\Delta^{\alpha\alpha}$ in homogeneous pair collisions of these species. For capsules of same V, all three shapes studied have similar l_d calculated from full simulation and predicted from theory, a reflection of their migration trend (or more precisely, lack thereof). Although it is not able to capture the precise values of l_d, the simple theory clearly captures the correct trends.

VI. CONCLUSIONS

In this work, we investigated the flow-induced segregation behavior in binary suspensions on neo-Hookean capsules subjected to simple shear flows in a planar slit. The two species in the suspension differ only in shape as characterized by their aspect ratio. Shape was varied by two approaches: (a) the two components had the same equatorial radius and their aspect ratio was varied to change shape (b) the two components had the same volume and their aspect ratio as well as equatorial radius was varied to change shape. The detailed boundary integral simulations revealed that when equatorial radius is held constant, capsules of lower aspect ratio marginate when present in trace amount in mixture dominated by higher aspect ratio capsules, while when volume is held constant, ellipsoidal capsules demarginate in mixture with spherical capsules.

A unifying trend between different segregation behaviors is presented in Sec. IV. Segregation can be understood to result from a competition between wall-induced migration of deformable capsules and shear-induced collisions. When equatorial radius is held constant, migration velocity at a wall-normal position is found to be proportional to aspect ratio, while it shows only a weak dependence on aspect ratio when volume is held constant. In heterogeneous pair collisions of capsules with same radius, the capsule having lower aspect ratio displaces more than the higher aspect ratio one. However, for capsules having the same volume, spherical particles displace more than ellipsoidal particles. These features of particle migration and pair-collisions shed significant light on the mechanistic insights which explains particle distribution in suspensions reported above. The recently-developed simplified drift-diffusion theory [48] was extended to understand shape-mediated segregation and was found to capture the key qualitative features of shape-segregation remarkably well.

The simplified drift-diffusion theory comprises substantial progress in the understanding and prediction of segregation behavior in multicomponent suspensions of deformable particles. As its input, it requires only migration, drift and diffusion coefficients, which can be obtained via simple experiments or computationally inexpensive simulations. The various margination regimes and the drainage transition predicted by the theory are seen in full simulations. The comprehensive study of how each of the individual physical aspects of cell deformability and size [5, 7] and shape (this work) lead to experimentally observed segregation behavior, and the corresponding theoretical framework [48] provide a foundation for the

understanding of flow-induced segregation in blood and applications such as lab-on-a-chip and targeted drug delivery. In these more complex systems different components differ in multiple properties (e.g. red and white blood cells differ in size, shape *and* flexibility); the results presented here help disentangle the effects of these various differences.

ACKNOWLEDGMENTS

This material is based upon work supported by the National Science Foundation under Grants No. CBET-1132579 and No. CBET-1436082 and a BP graduate fellowship granted to KS.

[1] R. Skalak, N. Ozkaya and T. C. Skalak, *Annu. Rev. Fluid Mech.*, 1989, **21**, 167–200.

[2] A. S. Popel and P. C. Johnson, *Annu. Rev. Fluid Mech.*, 2005, **37**, 43.

[3] G. Tangelder, H. C. Teirlinck, D. W. Slaaf and R. S. Reneman, *Am. J. Physiol.: Heart Circ. Physiol.*, 1985, **248**, H318–H323.

[4] J. C. Firrell and H. H. Lipowsky, *Am. J. Physiol.: Heart Circ. Physiol.*, 1989, **256**, H1667–H1674.

[5] A. Kumar and M. D. Graham, *Phys. Rev. E*, 2011, **84**, 066316.

[6] A. Kumar and M. D. Graham, *Soft Matter*, 2012, **8**, 10536–10548.

[7] A. Kumar, R. G. Henríquez Rivera and M. D. Graham, *J. Fluid Mech.*, 2014, **738**, 423–462.

[8] J. A. Champion and S. Mitragotri, *Proc. Natl. Acad. Sci. U. S. A.*, 2006, **103**, 4930–4934.

[9] J. A. Champion, Y. K. Katare and S. Mitragotri, *J. Controlled Release*, 2007, **121**, 3–9.

[10] S. E. Gratton, P. A. Ropp, P. D. Pohlhaus, J. C. Luft, V. J. Madden, M. E. Napier and J. M. DeSimone, *Proc. Natl. Acad. Sci. U. S. A.*, 2008, **105**, 11613–11618.

[11] S. Mitragotri and J. Lahann, *Nat. Mater.*, 2009, **8**, 15–23.

[12] F. Gentile, C. Chiappini, D. Fine, R. Bhavane, M. Peluccio, M. M.-C. Cheng, X. Liu, M. Ferrari and P. Decuzzi, *J. Biomech.*, 2008, **41**, 2312–2318.

[13] A. J. Thompson, E. M. Mastria and O. Eniola-Adefeso, *Biomaterials*, 2013, **34**, 5863–5871.

[14] R. Toy, P. M. Peiris, K. B. Ghaghada and E. Karathanasis, *Nanomedicine*, 2014, **9**, 121–134.

[15] S. Mitragotri, P. A. Burke and R. Langer, *Nat. Rev. Drug Discovery*, 2014, 1474–1776.

[16] Y. Geng, P. Dalhaimer, S. Cai, R. Tsai, M. Tewari, T. Minko and D. E. Discher, *Nat. Nanotechnol.*, 2007, **2**, 249–255.

[17] J.-W. Yoo, D. J. Irvine, D. E. Discher and S. Mitragotri, *Nat. Rev. Drug Discovery*, 2011, **10**, 521–535.

[18] P. Kolhar, A. C. Anselmo, V. Gupta, K. Pant, B. Prabhakarpandian, E. Ruoslahti and S. Mitragotri, *Proc. Natl. Acad. Sci. U. S. A.*, 2013, **110**, 10753–10758.

[19] N. Doshi, B. Prabhakarpandian, A. Rea-Ramsey, K. Pant, S. Sundaram and S. Mitragotri, *J. Controlled Release*, 2010, **146**, 196–200.

[20] P. Decuzzi, B. Godin, T. Tanaka, S.-Y. Lee, C. Chiappini, X. Liu and M. Ferrari, *J. Controlled Release*, 2010, **141**, 320–327.

[21] R. Toy, E. Hayden, C. Shoup, H. Baskaran and E. Karathanasis, *Nanotechnology*, 2011, **22**, 115101.

[22] G. Adriani, M. D. de Tullio, M. Ferrari, F. Hussain, G. Pascazio, X. Liu and P. Decuzzi, *Biomaterials*, 2012, **33**, 5504–5513.

[23] K. D. Young, *Microbiol. Mol. Biol. Rev.*, 2006, **70**, 660–703.

[24] P. Canham and A. C. Burton, *Circ. Res.*, 1968, **22**, 405–422.

[25] K. Chotivanich, R. Udomsangpetch, R. McGready, S. Proux, P. Newton, S. Pukrittayakamee, S. Looareesuwan and N. J. White, *Journal of Infectious Diseases*, 2002, **185**, 1538–1541.

[26] S. Sugaya, M. Yamada and M. Seki, *Biomicrofluidics*, 2011, **5**, 024103.

[27] M. Masaeli, E. Sollier, H. Amini, W. Mao, K. Camacho, N. Doshi, S. Mitragotri, A. Alexeev and D. Di Carlo, *Phys. Rev. X*, 2012, **2**, 031017.

[28] B. J. Peter, H. M. Kent, I. G. Mills, Y. Vallis, P. J. G. Butler, P. R. Evans and H. T. McMahon, *Science*, 2004, **303**, 495–499.

[29] H. T. McMahon and J. L. Gallop, *Nature*, 2005, **438**, 590–596.

[30] J. Zimmerberg and M. M. Kozlov, *Nat. Rev. Mol. Cell Biol.*, 2006, **7**, 9–19.

[31] B. Antonny, *Annu. Rev. Biochem.*, 2011, **80**, 101–123.

[32] D. S. Miller, X. Wang and N. L. Abbott, *Chem. Mater.*, 2013, **26**, 496–506.

[33] F. Mondiot, X. Wang, J. J. de Pablo and N. L. Abbott, *J. Am. Chem. Soc.*, 2013, **135**, 9972–9975.

[34] J. Tan, A. Thomas and Y. Liu, *Soft Matter*, 2012, **8**, 1934–1946.

[35] K. Müller, D. A. Fedosov and G. Gompper, *Sci. Rep.*, 2014, **4**, 4871.

[36] J. Tan, S. Shah, A. Thomas, H. D. Ou-Yang and Y. Liu, *Microfluid. Nanofluid.*, 2013, **14**, 77–87.

[37] C. Sun, C. Migliorini and L. L. Munn, *Biophys. J.*, 2003, **85**, 208–222.

[38] J. B. Freund, *Phys. Fluids*, 2007, **19**, 023301.

[39] D. A. Fedosov, J. Fornleitner and G. Gompper, *Phys. Rev. Lett.*, 2012, **108**, 028104.

[40] L. Crowl and A. L. Fogelson, *J. Fluid Mech.*, 2011, **676**, 348–375.

[41] H. Zhao and E. S. G. Shaqfeh, *Phys. Rev. E*, 2011, **83**, 061924.

[42] H. Zhao, E. S. Shaqfeh and V. Narsimhan, *Phys. Fluids*, 2012, **24**, 011902.

[43] D. A. Reasor Jr, M. Mehrabadi, D. N. Ku and C. K. Aidun, *Ann. Biomed. Eng.*, 2013, **41**, 238–249.

[44] J. Freund and B. Shapiro, *Phys. Fluids*, 2012, **24**, 051904.

[45] A. Kumar and M. D. Graham, *Phys. Rev. Lett.*, 2012, **109**, 108102.

[46] V. Narsimhan, H. Zhao and E. S. G. Shaqfeh, *Phys. Fluids*, 2013, **25**, 061901.

[47] M. Zurita-Gotor, J. Blawzdziewicz and E. Wajnryb, *Phys. Rev. Lett.*, 2012, **108**, 68301.

[48] R. G. H. Rivera, K. Sinha and M. D. Graham, *Phys. Rev. Lett.*, 2015, **114**, 188101.

[49] D. Barthes-Biesel, A. Diaz and E. Dhenin, *J. Fluid Mech.*, 2002, **460**, 211–222.

[50] J. M. Charrier, S. Shrivastava and R. Wu, *J. Strain Anal. Eng. Des.*, 1989, **24**, 55–74.

[51] A. Kumar and M. D. Graham, *J. Comput. Phys.*, 2012, **231**, 6682–6713.

[52] P. Pranay, S. G. Anekal, J. P. Hernandez-Ortiz and M. D. Graham, *Phys. Fluids*, 2010, **22**, 123103.

[53] E. Lac, A. Morel and D. Barthès-Biesel, *J. Fluid Mech.*, 2007, **573**, 149–169.

[54] J. Sherwood, F. Risso, F. Collé-Paillot, F. Edwards-Lévy and M. C. Lévy, *J. Colloid Interface Sci.*, 2003, **263**, 202–212.

[55] C. Pozrikidis, *Boundary Integral and Singularity Methods for Linearized Viscous Flow*, Cambridge University Press, 1992.

[56] J. P. Hernandez-Ortiz, J. J. de Pablo and M. D. Graham, *Phys. Rev. Lett.*, 2007, **98**, 140602.

[57] H. Flyvbjerg and H. G. Petersen, *J. Chem. Phys.*, 1989, **91**, 461–466.

[58] X. Li and C. Pozrikidis, *Int. J. Multiphase Flow*, 2000, **26**, 1247–1279.

[59] S. D. Hudson, *Phys. Fluids*, 2003, **15**, 1106–1113.

[60] P. Pranay, R. G. Henriquez Rivera and M. D. Graham, *Phys. Fluids*, 2012, **24**, 061902.

[61] J. R. Smart and D. T. Leighton Jr, *Phys. Fluids*, 1991, **3**, 21–28.

[62] H. Ma and M. D. Graham, *Phys. Fluids*, 2005, **17**, 083103.

[63] D. Barthes-Biesel and V. Chhim, *Int. J. Multiphase Flow*, 1981, **7**, 493–505.

[64] F. R. daCunha and E. J. Hinch, *J. Fluid Mech.*, 1996, **309**, 211–223.